

LOW TEMPERATURE SCANNING TUNNELING MICROSCOPY AND SPECTROSCOPY IN ULTRA-HIGH-VACUUM AND HIGH MAGNETIC FIELDS

THÈSE N° 1780 (1998)

PRÉSENTÉE AU DÉPARTEMENT DE PHYSIQUE

ÉCOLE POLYTECHNIQUE FÉDÉRALE DE LAUSANNE

POUR L'OBTENTION DU GRADE DE DOCTEUR ÈS SCIENCES

PAR

Andreas HIRSTEIN

Diplom-Physiker, Rheinische Friedrich-Wilhelms-Universität, Bonn
de nationalité allemande

acceptée sur proposition du jury:

Prof. K. Kern, directeur de thèse
Prof. R. Berndt, corapporteur
Prof. G. Comsa, corapporteur
Dr R. Gotthardt, corapporteur

Lausanne, EPFL
1998

Version abrégée

Un microscope à effet tunnel pour utilisation à basses températures (LTSTM) a été développé afin de réaliser des mesures spectroscopiques locales ainsi que la manipulation directe des atomes. La construction du microscope est basée sur le principe de Besocke et permet l'installation du LTSTM à l'intérieur d'un cryostat à l'hélium liquide dans un environnement du ultra-haut vide(UHV). L'utilisation de matières non-magnétiques permet de travailler dans un champ magnétique jusqu'à 5 T.

En comparaison avec le microscope du type "beetle", la nouvelle construction est caractérisée par des fréquences propres élevées et une meilleure stabilité mécanique. En combinaison avec un système d'isolation de vibrations à trois étages, le LTSTM peut être utilisé pour des mesures à haute résolution. La résolution atomique de surfaces métalliques compactes est couramment obtenue. Un blindage thermique inhérent limite la dérive thermique à moins de 2 Å/h. Le microscope est calibré par des images à résolution atomique de la surface reconstruite de Au(110) à des températures de 300 K, 77 K et 5 K.

La préparation de l'échantillon se fait dans le vide, *in situ*, sur un manipulateur à température variable. Le système est équipé de systèmes standards pour la préparation et l'analyse de surface.

Le transfert de l'échantillon dans le vide se fait par un système de manipulation comprenant un sas pour échanger l'échantillon sans être obligé de casser le vide.

Le microscope a été utilisé pour étudier l'état électronique de surface de Ag(111) à 5 K par des mesures topographique (STM) ainsi que spectroscopique (STS). La diffusion des électrons de l'état de surface par des défauts localisés à la surface a été observée en mode topographique. Les données spectroscopiques montrent que l'état de surface existe à partir de 65 meV au-dessous de l'énergie de Fermi. Par spectroscopie locale la relation de dispersion de l'état de surface a été déterminée. Il se trouve que l'état de surface forme un gaz bi-dimensionnel d'électrons approximativement libre

d'une masse effective $m^* = 0.41m_e$. Il est montré qu'une paire de marches parallèles constitue une structure qui, en confinant les électrons, crée un spectre discret. Finalement la structure d'îlots de nickel et leur influence sur l'état de surface est présentée.

Abstract

We have developed an ultra-stable low temperature scanning tunneling microscope (LTSTM) for application in atomic scale spectroscopy and atom manipulation experiments. The design is based on the Besocke type microscope allowing the installation of the LTSTM within a liquid helium bath (*LHe*) cryostat in ultra-high-vacuum (UHV). The exclusive use of nonmagnetic materials allows STM-operation in magnetic fields up to 5 T without influencing the measurements.

Compared to the frequently used “beetle” type STM the new design is characterized by increased eigenfrequencies and an improved mechanical stability. In conjunction with a triple-stage vibration isolation system the LTSTM is suited for high resolution measurements. Atomic resolution on close-packed metal surfaces is routinely achieved. Inherent thermal shielding of the complete tunneling assembly minimizes thermal drift to less than 2 Å/h. The microscope is calibrated by means of atomic resolution images of the “missing-row” reconstructed Au(110) surface at temperatures of 300 K, 77 K and 5 K.

Sample preparation takes place on a variable temperature manipulator *in situ* in UHV. The system is equipped with standard surface preparation and analysis tools.

Sample transfer to the STM is performed in UHV by a sample transfer system that includes as well a fast-load-lock for sample exchange without breaking the main vacuum.

The microscope has been used to study the electronic surface state of Ag(111) at 5 K by topographic (STM) and spectroscopic (STS) measurements. The scattering of the surface state electrons off surface defects has been observed in topographic measurements. The spectroscopic data show the onset of the surface state at 65 meV below the Fermi energy. By locally resolved tunneling spectra the electron dispersion relation of the surface state has been determined. The data reveal that the surface state forms a nearly free, two-dimensional electron gas with an effective mass m^* of the surface

state electrons $0.41m_e$. A pair of parallel surface steps acting as confining structures has been shown to cause a discrete spectrum of confined states. Finally, the structure of Ni adislands and their influence on the surface state are presented.

Contents

1	Introduction	1
2	Electron tunneling	7
3	Experimental	13
3.1	Some considerations on vibration isolation	13
3.2	Specification of the STM	19
3.3	The UHV-chamber and vibration isolation	21
3.4	The cryostat	26
3.5	The low temperature STM	29
3.5.1	Description of the design	29
3.5.2	Characterization of the STM	34
3.6	The sample manipulation and transfer system	44
3.6.1	The sample holder	44
3.6.2	The variable temperature manipulator	46
3.7	Sample preparation and imaging conditions	49
3.7.1	Sample preparation	49
3.7.2	Imaging conditions	49
4	STM calibration on Au(110)	51
4.1	The Au(110) surface	51
5	Surface States on Ag(111)	61
5.1	The surface state on Ag(111)	61
5.2	The surface state dispersion relation	65
5.3	Spatially confined surface states	72
6	Ni islands on Ag(111)	77
6.1	The structure of Ni islands on Ag(111)	78
6.2	Tunneling spectra on Ni islands	84

7 Outlook	87
Curriculum vitae	95
Remerciements	97

Chapter 1

Introduction

The origin of ferromagnetism and superconductivity is a very dissimilar behavior of electrons in the solid. While the former is caused by the “spin-spin” interaction of the electrons of an incomplete inner shell of atoms in the solid the latter effect arises from the formation of electron pairs with opposing spins that is mediated by the “electron-phonon” interaction in the crystalline lattice. However, both effects reside on the bulk properties of the solid state. Therefore the question arises how the magnetic and superconducting properties would change if the spatial dimensions of the solid were reduced to a range smaller than some characteristic length scales such as the electron coherence length ξ_0 [1]. For superconductivity it has been predicted (the so called Anderson criterion) that it ceases when the spatial confinement of the electrons in the particle leads to discrete energy levels that are separated from each other by an amount bigger than the superconducting order parameter [2].

Experiments focusing on this question have been performed since the 1960s. Giaever and Zeller employed electron tunneling in order to determine whether small tin particles embedded in an oxide matrix are superconducting or not [3]. They found that the grains stayed superconducting down to an average size of 25 Å. The critical magnetic field H_c was found to be proportional to $1/r$.

Electron tunneling experiments are well suited to study the electron density of states since under certain assumptions the density distribution is mapped by the derivative dI/dV of the tunneling current (see chapter 2). The measurements suffered, however, from an other drawback. Since the tunneling current was not transmitted through solely one isolated particle the current always included information from many particles with different size and shape and represented therefore an average over a size distribution

which was not completely uniform.

The situation is more favorable in studies of thin superconducting films [4, 5]. To produce a superconducting electrode with a suitable tunnel junction aluminum has most extensively been used because its natural oxide layer Al_2O_3 is chemically self-limiting in a range required for tunneling. It turned out that the properties of superconducting Al films change dramatically from the behavior of bulk Al [6]. As a further experimental simplification the transition temperature T_c of Al rises from 1.18 K in the bulk to 2.5 K in thin films. Even more pronounced is the change of the critical magnetic field H_c which increases depending on the field direction with respect to the film plane by several orders of magnitude. The latter is due to an incomplete Meissner effect in thin films. In the bulk circulating surface currents lead to a complete expulsion of the magnetic field from the superconductor. These currents cost energy and lead therefore to the breakdown of the superconducting state at the critical field H_c . When the thickness d of the superconducting film becomes smaller than the penetration depth λ that is, smaller than the thickness of the surface layer where the screening currents flow, the external field penetrates the entire film. Accordingly, the screening currents are much smaller than in the bulk and the energy rise is minimum. The critical field of thin superconducting films therefore becomes a function of the film thickness. For fields applied parallel to the film one found a $d^{-3/2}$ dependence of H_c .

This effect has important experimental consequences. In magnetic fields of several Tesla the Zeeman splitting in the density of states can be observed. Each peak of occupied and unoccupied states of the BCS density of states of the superconductor then splits into two maxima corresponding to the spin-up and the spin-down state. Symmetrically around zero energy the density of states is therefore characterized by two pairs of maxima and each pair contains a peak of spin-up and one peak of spin-down electrons.

Tedrow and Meservy [6] were the first who measured the tunneling conductance between such a superconducting film and a ferromagnetic nickel counterelectrode. Since the density of states in the Ni electrode is different for spin-up and spin-down electrons the total tunneling current is polarized in the direction of the majority spins. Consequently, the tunneling conductance becomes asymmetric around zero energy due to the spin splitting in the superconducting Al electrode. The tunneling current can therefore be employed to test whether one sample electrode is ferromagnetic or not. Adopting this method to scanning tunneling spectroscopy (STS) would provide the possibility to investigate the magnetism on the local scale. However, the critical

field of the superconducting electrode needs to be very high (in the order of several Tesla) in order to create a measurable spin splitting in the density of states.

In a recent study Yazdani *et al.* [7] have demonstrated a method that allows to distinguish magnetic from non-magnetic adsorbates by the influence of a magnetic moment on the density of states on a superconductor. Tunneling spectra obtained near magnetic impurities on a superconducting Nb sample showed the presence of excitations within the energy gap of the superconductor. At nonmagnetic impurities these excitations were absent. Thereby it has become possible to distinguish magnetic from nonmagnetic adsorbates on the atomic scale by STS.

The above mentioned difficulty to produce tunnel junctions between external leads and a single nanoscopic particle has recently been overcome by Ralph, Black and Tinkham [8, 9]. By their sample preparation technique a small Al particle (≤ 10 nm) is connected via two Al_2O_3 junctions to external superconducting Al leads. From the conductance of the double barrier setup (two successive tunneling junctions) it has been possible for the first time to resolve discrete energy levels of a single metal particle. The size of the particle is not directly accessible and has to be calculated from the capacity of the tunneling assembly. This procedure is rather cumbersome as for each measurement a completely new sample has to be prepared. With the advent of the scanning tunneling microscope (STM) [10] an alternative technique exists. Its high spatial resolution offers the possibility to select single nanoscopic particles adsorbed on the sample surface that can subsequently be investigated by means of tunneling spectroscopy. Several research groups have demonstrated the STM can as well be used in double barrier tunneling junctions [11, 12, 13, 14, 15]. In this case the particle to be investigated is adsorbed on an isolating surface layer that has been grown on the sample crystal.

Moreover, since Eigler and coworkers [16] have demonstrated the capability of the STM to manipulate single atoms by means of the tunneling tip and to construct artificial structures on the surface, tunneling microscopy is not restricted any more solely to analysis objectives but can be employed as well as a sample preparation tool.

The technical demands to the instrument are however very high and only very few microscopes exist that have been proven to be capable to manipulate single atoms in a controlled manner. As will become clear from chapter 3 the STM will necessarily have to operate at low temperature in order to achieve a very high mechanical stability of the tunneling assembly and to reduce

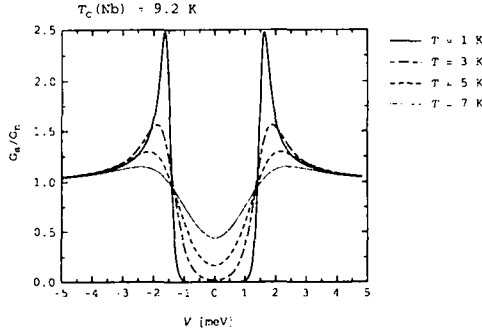


Figure 1.1: Theoretical density of states of a conventional superconductor (Nb) calculated by the model of Bardeen, Cooper and Schrieffer (BCS) [17].

thermal drift to a minimum level. Otherwise the resolution of features in the electron density of states that are often in the range of a millivolt (see the density of states gap of a conventional superconductor in Figure 1.1) could not be resolved. (Obviously, in the study of superconductors a low temperature set-up is already necessary to render the sample superconducting.)

The aim of the present thesis was therefore to design and build an ultra-stable low temperature scanning tunneling microscope (LTSTM) with an improved mechanical stability as compared to other so-called beetle type STMs that can be integrated in an helium bath cryostat. The microscope must operate in UHV in order to guarantee clean and reproducible tunneling conditions. The STM operation must not be influenced by magnetic fields of up to 5 Tesla that can be used to drive phase transitions in the sample.

The thesis is divided as follows. In the following chapter a short synopsis of electron tunneling theory is given. It focuses on the question how spectroscopic information can be obtained from the measurement. Starting from the definition of the performance requirements chapter 3 presents a detailed description and characterization of the LTSTM-system. The resolution performance of the microscope is demonstrated in chapter 4 by experiments on a “missing-row” reconstructed Au(110) surface.

The surface state on Ag(111) forms a nearly free electron gas established by electrons that are confined in a plane parallel to the surface. In chapter 5 the dispersion relation of the surface state is determined from tunneling spectroscopy. In mesoscopic clusters a further confinement of the electrons by

lateral boundary conditions leads to discrete energy levels in the respective direction. A similar behavior is shown by an example of two parallel surface steps which can limit the lateral electron motion by partial reflection.

In the final chapter the structure of Nickel islands grown on the Ag(111) surface is studied and the effect of adsorbed Ni on the surface state of Ag(111) is investigated by scanning tunneling spectroscopy (STS).

Chapter 2

Electron tunneling

The partial transmission of an electron wave in a metal through the potential barrier of the vacuum is known as the tunneling effect of the electron. It is due to the physical necessity that the wave functions and their derivatives are continuous at the boundaries of the solid. To obtain a finite probability of the tunneling event the barrier width has to be small. This can be accomplished either by applying a high electrical field as in field emission [18] or by approaching a second metal that deforms the vacuum barrier between the two electrodes to a potential well of finite width. This second possibility has been realized in scanning tunneling microscopy [10] where one electrode is established by a sharp metal tip that probes locally the sample surface. By scanning the tip linewise over a small region on the surface a locally resolved two dimensional representation of electronic surface properties can be acquired.

Upon applying a potential difference between the two electrodes (tip and sample) a net current flows. As discussed below the tunneling current maps under certain conditions the density of states of one electrode (the sample).

In order to find this dependence two basic approaches have been developed. The transfer Hamiltonian approach originally used by Oppenheimer has been adopted to tunneling microscopy by Tersoff and Hamann [19, 20]. Based on the calculation of Bardeen [21] for tunneling between two parallel plates separated by an insulator Tersoff and Hamann first calculated the wave functions of the tunneling tip and the sample in solving separately their time independent Schrödinger equation. Using time-dependent perturbation theory one gets

$$I = \frac{2\pi}{\hbar} \sum_{\mu, \nu} \{f(E_\mu)[1-f(E_\nu)] - f(E_\nu)[1-f(E_\mu)]\} |M_{\mu,\nu}| \delta(E_\nu + eV - E_\mu), \quad (2.1)$$

where $M_{\mu,\nu}$ is the tunneling matrix element between the states Ψ_μ and Ψ_ν of the tip and the sample, V the applied voltage, and $f(E)$ the Fermi function. The crucial factor of this equation is the tunneling matrix element. Since it is a convolution of tip and sample states the physical properties of both will enter in a symmetrical manner and information of the sample is not easy to obtain. Therefore Tersoff and Hamann modeled the tip as a point source without any electronic structure. Furthermore, especially in low temperature experiments the assumption of zero temperature is justified. The further restriction to small tunneling voltages leads to the expression,

$$I \propto \sum_{\nu} |\Psi_{\nu}(r_t)|^2 \delta(E_{\nu} - E_F) = \rho(r_t, E_F), \quad (2.2)$$

where r_t is the location of the tunneling tip.

In this expression the current is proportional to the local density of states of the sample. Comparison with experiment shows that this result is a good approximation for tips with s-wave-like states. However, experimentally obtained atomic resolution cannot be recovered from the calculation.

Refinements of the theory [22] that take into account in a more detailed manner sample and tip states have only been successful in some special cases. A model which were generally applicable to explain atomic resolution on metals is still lacking.

A second approach to calculate the tunneling current is based on a calculation that was originally used in 1928 by Gamow to describe the alpha decay of radioactive heavy nuclei. Following the description of Wolf [23] its details are presented in the following. Finally, the model is applied to the case of a simplified two dimensional electron gas observed on the Ag(111) surface.

Let us consider the one dimensional barrier as indicated in Figure 2.1. Then the wave function can be separated into a transverse and a parallel part with respect to the tunneling direction. This can be described as

$$\Psi = \psi_x \psi_p,$$

where ψ_p is a two dimensional plane wave and ψ_x , the transverse part, is oscillatory in region 1 and 2 and exponentially decaying in between.

For a simple rectangular potential well the decay constant,

$$\kappa_0 = \left(\frac{2m}{\hbar^2} \right)^{1/2} [U - E]^{1/2}, \quad (2.3)$$

would become independent of x (since $U(x)$ is constant) and the transmission factor as well as the current itself would be proportional to the exponential

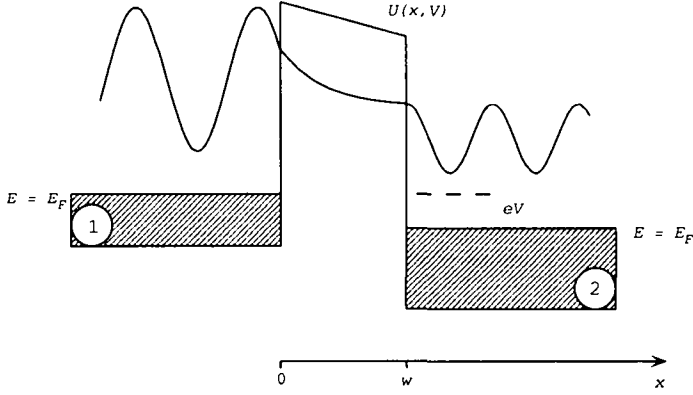


Figure 2.1: One dimensional model of the tunneling barrier. $U(x)$ is the tunneling barrier between the two metal electrodes 1 and 2. The transverse part of the wave function and its derivative are smooth at the boundaries of the barrier.

$e^{\kappa_0 w}$, where w is the width of the barrier. In the general case the decay constant κ has to be calculated for each x and the transmission factor D can be represented as

$$D(E_x) = g e^{-2K}, \quad (2.4)$$

where K is defined through

$$K = \int_0^w \kappa(x, E_x) dx, \quad (2.5)$$

and

$$\kappa(x, E_x) = \left(\frac{2m}{\hbar^2} \right)^{1/2} [U(x) - E_x]^{1/2}. \quad (2.6)$$

Once the transmission factor of the problem is known the current flowing from electrode 1 to electrode 2 can be calculated as the integral over all available k states weighted by the group velocity perpendicular to the barrier and the Fermi function for occupied states in 1 and unoccupied states in 2:

$$I_{1 \rightarrow 2} = \frac{2e}{(2\pi)^3} \iiint d^2 k_p dk_x \left(\frac{1}{\hbar} \frac{\partial E}{\partial k_x} \right) D f(E) [1 - f(E + eV)]. \quad (2.7)$$

For the opposite tunnel direction one obtains a similar expression. The net current is then calculated as the difference between these two contributions:

$$I = \frac{2e}{(2\pi)^2 h} \int_0^\infty dE_x [f(E) - f(E + eV)] \iint d^2 k_p D(E_x, V), \quad (2.8)$$

where the relation

$$dk_x = \frac{\partial k_x}{\partial E_x} dE_x \quad (2.9)$$

has been inserted. From equation (2.6) it is obvious that the transmission factor D is peaked around $k_p = 0$ since E_x becomes maximum for these states. However, the tunneling current between the electrodes is not purely perpendicular to the surface because also states with $k_p \neq 0$ contribute to it. In an approximation used for parallel plates Wolf [23] shows that the transmission factor D decreases to De^{-1} at a tunneling angle of eight degrees. From a treatment of Kashiwaya [24] follows that the tunneling filament becomes even more dispersed in space when one of the electrodes is replaced by a tip with small lateral dimensions. Besides the fact that atomic corrugation increases at small distances from the sample surface, this effect gives a further hint why in STM a small tip-sample separation is important to enhance the lateral resolution.

In Figure 2.2 the Fermi surface of an ideal 2D free electron gas on a metal surface is shown. Since only states with $k_x = 0$ exist the integration over k_x can be dropped. By the choice of appropriate boundaries of the integral in eq. 2.8 the current results to

$$I(V) = \frac{2e\rho_p}{h} D(E_x, V) \int_{E_F - eV}^{E_F} dE_t = \frac{2e^2}{h} V \rho_p D(E_t, V), \quad (2.10)$$

where the two-dimensional density of states ρ_p is defined by

$$\frac{d^2 k_p}{(2\pi)^2} = \rho_p dE_p. \quad (2.11)$$

Consequently, the conductance is linearly proportional to the density of states of the surface state:

$$\frac{\partial I}{\partial V} = \frac{2e^2}{h} \rho_p D(E_t, V). \quad (2.12)$$

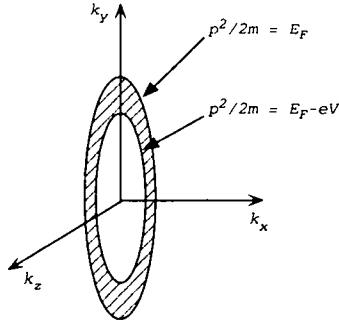


Figure 2.2: Sketch of Fermi circle of a 2D electron gas. States contributing to the tunneling current under bias V are hatched.

As has been noted by Renner [25], by measuring the conductance perpendicular to the barrier one is hence able to probe the density of states of a 2D electron gas with wave vectors parallel to the barrier. This is the case for surface states on close-packed noble metal surfaces such as Au(111), Ag(111) and Cu(111). The case of Ag(111) is discussed in chapter 5.

Chapter 3

Experimental

3.1 Some considerations on vibration isolation

From inspection of equation (2.4) it becomes obvious that the transmission factor D and consequently the tunnel current I depends exponentially on the barrier width. As a rule of thumb one says that varying the distance between tip and sample by 1 Å changes the current by one order of magnitude. In order to gain topographical or spectroscopic information about the sample it is therefore necessary to control the relative movement between tip and sample better than the required resolution e.g. if one wishes to obtain 1/100 Å resolution along z , a stability of the microscope better than 1/1000 Å is needed.

Basically, there are two sources of vibration noise from the environment. First building vibrations mostly in the frequency range between 10 and 100 Hz are typically of the order of several thousand Angstrom. Therefore these vibrations have to be damped by a factor of 10^6 . Secondly, sound from laboratory equipment can also excite mechanical vibration of the microscope. Its frequency range extends up to several kilohertz. The attenuation of vibrations can generally be achieved by two strategies.

The first one is to rise the lowest eigenfrequency of the tunneling assembly by increasing its stiffness in a way that the corresponding transfer function becomes smaller than 10^{-6} in the relevant frequency range.¹ Additionally, if the first strategy is not sufficient, one has to isolate the microscope from vibration.

¹The transfer function of a mechanical system is defined by the ratio between its vibration amplitude and the amplitude of the excitation.

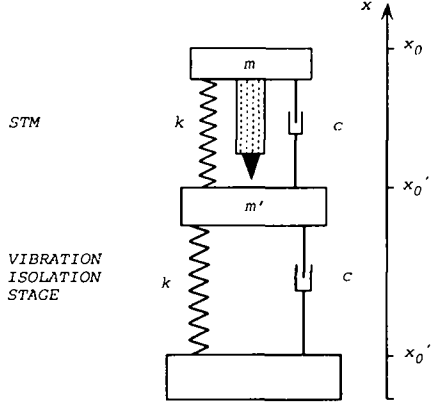


Figure 3.1: Harmonic model of a tunneling assembly. k denotes the spring constants and c the damping constants.

Estimations by Park [26] show that in order to achieve the aforementioned damping requirement for all frequencies smaller than 200 Hz an eigenfrequency of at least 200 kHz of the microscope would be necessary. Since already the lowest eigenfrequencies of piezoceramics are usually smaller than 10 kHz such a value is not achievable. Moreover certain minimum dimensions are required to accommodate for the sample holder in the microscope. This demand also lowers the eigenfrequencies of the system. Therefore in the frequency range beginning at 2 Hz the system has additionally to be isolated from vibrations (the second strategy).

To understand the principles of vibration isolation one usually models the system by coupled one-dimensional harmonic oscillators. Figure 3.1 shows the respective drawing for the tunneling assembly and one vibration isolation stage. The quantity of interest is the tunneling gap distance $(x_0 - x_0')$ or more precisely the dependence of this distance from external vibrations. From the solution of the equation of motion one can calculate the corresponding transfer function for the tunneling gap:

$$|T_1(f)| := \left| \frac{x_0 - x_0'}{x_0'} \right| \quad (3.1)$$

This curve is plotted in Figure 3.2 where the abscissa shows the driving frequency in units of the resonant frequency ω_0 of the isolation stage and the

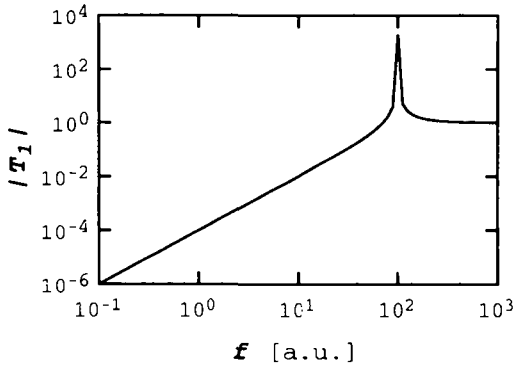


Figure 3.2: Transfer function of the tunneling gap distance ($x'_0 - x_0$).

ordinate the respective response of the tunneling gap in a case where $c = 0$. The assumption has been made that the resonance frequency of the STM is two orders of magnitude higher than the resonance of the vibration isolation system.

For frequencies sufficiently smaller than the resonant frequency, decreasing the excitation frequency by one order of magnitude causes the response amplitude to decrease by two orders. Similarly, one calculates the transfer function of the isolation stage to

$$|T_2(f)| = \left| \frac{x'_0}{x''_0} \right| \quad (3.2)$$

Figure 3.3 shows the behavior of this function. It is the behavior of a standard harmonic oscillator.

To obtain the overall response of the tunneling gap for the coupled system one has to multiply the transfer functions of the individual stages. The result is plotted in Figure 3.4 as a function of the resonance frequency of the tunneling device which in this case is supposed to be two orders of magnitude bigger than the resonance of the isolation stage. External vibration in the regime between the two eigenfrequencies is generally damped by a factor of 10^{-4} . Since this might not be sufficient for high resolution experiments further improvements are needed. If the most simple solution just to increase the difference of the resonance frequencies is not applicable due to other design constraints (e. g. space for the sample holder, possibility of lateral displacement of the STM with respect to the sample surface) one is

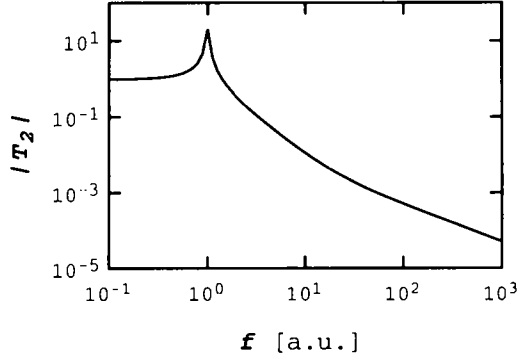


Figure 3.3: Transfer function of one isolation stage.

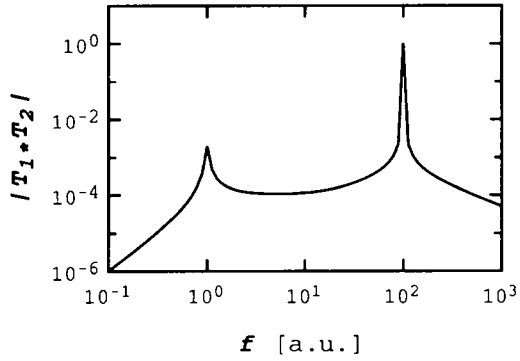


Figure 3.4: Total transfer function of the tunneling assembly.

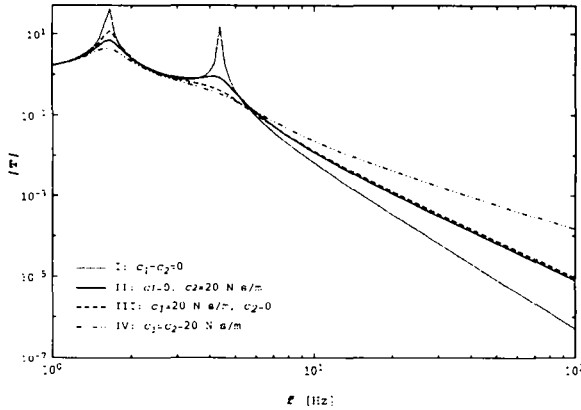


Figure 3.5: Transfer functions of a two stage vibration isolation system for different placements of dampers (c_1, c_2 are the damping constants in the first and second stage, respectively). The best performance is achieved by placing a damper only in the second stage (curve II). From [27].

forced to introduce a second vibration isolation stage. The corresponding transfer function for such a system can be calculated in exactly the same way as before. Okano [27] obtained the results depicted in Figure 3.5. Again the situation in the high frequency regime is best without damping in both isolation stages. However, the system's behavior close to the resonances is worse. Note that the best compromise is obtained when damping is present only in the second stage. In this arrangement excitation in the entire frequency range are sufficiently damped out. As was pointed out by Park [26] a double stage system has additional advantages which are not included in the above description of ideal harmonic oscillators. High frequency vibrations for instance can be transmitted through the spring wires to the tunneling microscope. The use of an intermediate mass between the two spring stages can prevent this. Another helpful measure is to clamp electrical or any other type of mechanical link from the outside world to the intermediate isolation stage.

The above picture of the tunneling microscope as a system of coupled harmonic oscillators is highly simplified. Especially in designs using some kind of inertial coarse approach the behavior of the mechanical contact responsible for the approach motion cannot be approximated with a harmonic potential. In a recent paper Behler *et al.* [29] characterized the mechanical resonances of

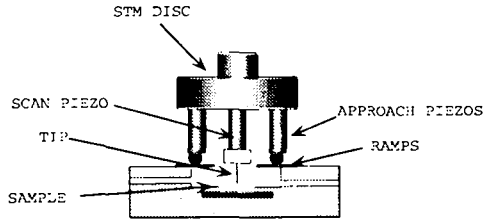


Figure 3.6: The standard beetle type microscope by Frohn et al. [28].

a standard beetle type microscope (see Figure 3.6). The intrinsic mechanical resonances of the scan head (e. g. bending modes of the piezo tubes) can indeed be described by harmonic oscillators. The corresponding frequencies are in the range of about 4 kHz. However, they are not the limiting factor of the microscope. Other vibrations related to a “rattling” motion of the scan head with respect to the ramp can impose more severe restrictions as they appeared between 500 and 1700 Hz. This frequency range is particularly important for atomic resolution images. From their dependence on the actual position of the scan head on the ramp it becomes obvious that the quality of the microcontact between the sapphire balls at the exterior piezo tubes and the ramps are of crucial importance in any design employing “stick and slip”-like coarse approach. The simplest way to address this point might be by increasing the weight of the scan head or more general the weight of the moving part of the STM. In section 3.5.2 we will see if this strategy can be successful.

3.2 Specification of the STM

As has been lined out in the introduction the purpose of the microscope described here is to perform high resolution measurements of both sample topography and electronic properties. Besides such purely analytical use the scanning tunneling microscope has also been used as a manipulation tool for single atoms or molecules adsorbed on the surface [30, 31]. The analysis of electronic features, for instance the resolution of the density of states gap in a normal superconductor, as well as manipulation experiments impose extreme demands on the stability of the instrument. Most probably, we will need a vertical stability of $\delta z \simeq 1 \text{ pm} = 1/100 \text{ \AA}$. Furthermore, temperature drift of the microscope also modifying the tunneling barrier width in time has to be reduced to a minimum level. In variable temperature designs that compensate to first order for temperature variations values of $\Delta \dot{x}$ and $\Delta \dot{z}$ of $1\text{-}10 \text{ \AA/s}$ can be achieved at room temperature. Typically, an STM has dimensions of about 30 mm. Since thermal expansion coefficients at room temperature are of the order of 10^{-5} K^{-1} the demand to keep the drift smaller than $1/100 \text{ \AA/s}$ would require a temperature stability of

$$\dot{T} = \frac{\Delta z}{\Delta \alpha l} \simeq 10^{-4} \text{ K/s.}$$

This is a value that can hardly be realized. The best way to solve the problem is therefore to perform experiments at low temperature by cooling the entire microscope and the sample to liquid helium temperature since this decreases the thermal expansion coefficients by several orders of magnitude. For atom manipulation experiment the cooling of the sample is also necessary to eliminate thermal activated diffusion of the atoms.

Both requirements (high resolution and low temperature) constitute the main design constraints. They cannot be considered independently since many materials change their mechanical properties at low temperatures. This concerns firstly the vibration isolation system because almost all materials which could be used for damping purposes lose their flexibility when being cooled to liquid Helium temperatures. This rules out the possibility to use any viscoelastic silicone or "Viton" rubber elements. Other desired features of the microscope can interfere with each other as well:

- The STM will operate in high magnetic fields. Obviously, all STM-materials have to be non-magnetic. Otherwise field inhomogeneities and drift problems could be a consequence. Secondly, the nowadays currently employed eddy-current damped spring suspension of the mi-

croscope must also be rejected as it would not work properly in variable magnetic fields.

- To obtain acceptable times between sample preparation and tunneling measurements a good thermal contact between the sample and the cryostat is needed. In this aim a firm mechanical contact is unavoidable.
- Additionally, one would like to have the possibility of lateral movement of the scan head with respect to the sample in order to investigate different regions of the sample. This limits the dimensions of the microscope to a certain minimum value. As a result the eigenfrequencies of the microscope will be limited by this constraint.
- To be able to determine the position of the scan head or to allow in situ optical measurements it would be helpful to have an optical access to the tip region. Thereby thermal radiation could lead to drift of the tunnel current.

In the following sections of this chapter it will become clear that the actually chosen design of the instrument is the result of a trade-off between the aforementioned requirements.

3.3 The UHV-chamber and vibration isolation

As has been mentioned in section 3.2 vibration isolation with adequate damping is hardly to achieve at low temperatures in a magnetic field. The additional requirement to establish a good thermal contact between cryostat and the sample led to the decision to reject any decoupling in the cryostat. On the contrary, the link has been chosen to be as rigid as possible. This has been done in order to guarantee high eigenfrequencies and an optimum thermal anchoring of the STM body.² As a consequence mechanical decoupling from the building has been realized in three successive stages outside the UHV-chamber.

Figure 3.7 shows an overview of the entire system. The UHV-chamber resides on a heavy stone plate which itself is suspended on the ceiling of the laboratory by means of large springs. This is the first isolation stage. The second one is situated between the stone plate and the UHV-chamber and consists of four standard pneumatic dampers[32]. Additionally, the UHV-chamber and the cryostat (on the right hand side of Figure 3.7) are decoupled by a flexible bellows of 300 mm inner diameter. Again pneumatic dampers are used to compensate for the weight of the cryostat and the force of the air pressure on the bellows.

The performance of this triple vibration isolation system can roughly be estimated by solving numerically the equations of motion as given by Okano [27]. In this calculation the spring suspension as well as the pneumatic dampers have been considered to be simple one dimensional damped harmonic oscillators. The spring and damping constants have been chosen to reflect approximately the properties (masses, spring and damping constants) of the individual components. The corresponding values are listed in table 3.1.

In Figure 3.8 the resulting spectra from the numerical solution of the equations of motion with the parameters as given in table 3.1 is shown. The damping of the three stages of the system in a range beginning at 100 Hz where eigenmodes of the STM could exist, is always better than 10^{-7} . At the resonances of the piezo tubes of 10 kHz the damping has decreased to a factor of 10^{-16} . This calculation gives only a rough estimation of the damping performance since it is based on a simplified model with parameters that are not known exactly. However, it indicates that the vibration isolation from

²Due to the design of the cryostat helium exchange gas as a cooling means would destroy the UHV of the complete system. See section 3.4

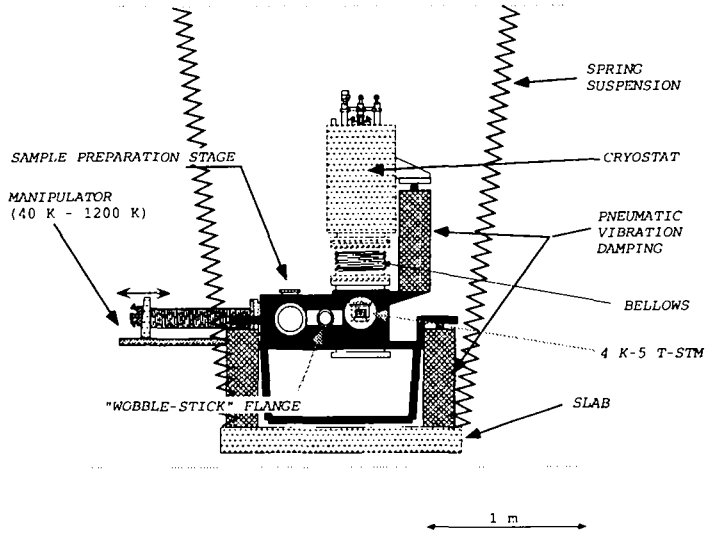


Figure 3.7: Setup of the UHV-chamber with three stages of vibration isolation.

Stage	Mass [kg]	Spring constant [N/m]	Damping constant [N s/m]
1	700	7500	0
2	700	50000	200
3	1000	50000	200

Table 3.1: Properties of the triple vibration isolation system. Assignments: 1 Stone plate; 2 UHV-chamber; 3 Cryostat (the mass includes the forces imposed by the air pressure on the flexible 300 mm inner diameter bellows).

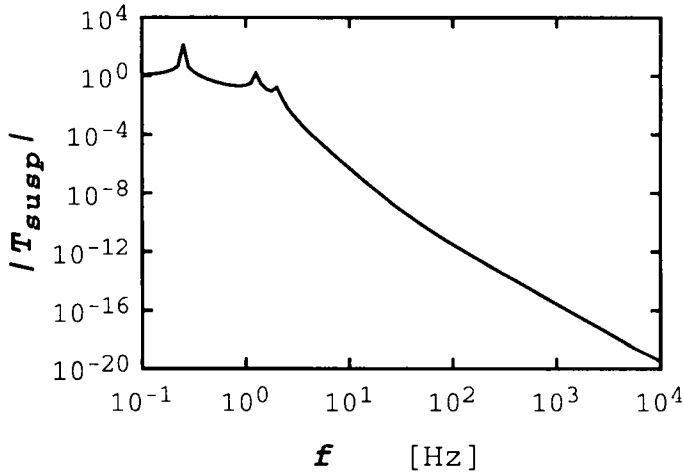


Figure 3.8: Transfer function of the triple vibration isolation system

the building should be sufficient.

The exclusive vibration isolation outside the cryostat has the drawback that sound which is picked up by the chamber walls cannot be eliminated. It will be transmitted through the stiff link between cryostat and STM and can limit the attainable resolution. Therefore the complete UHV experimental setup has been encapsulated by a sound insulation cubicle. The sound insulation is typically 40 dB averaged over the frequency range between 100 and 5000 Hz. All supply lines for the experiment are passed through special feedthroughs since any sound leak can limit the performance considerably. This is particularly important for the spring suspension where tubular sound absorbers for each spring have been installed.

If we take a closer look of Figure 3.7 we recognize on the left hand side of the chamber the variable temperature manipulator. With this manipulator (for details see 3.6.2) all sample preparation and analysis procedures prior to transferring the sample into the STM can be performed. It has three translational and one rotational degree of freedom. In the center of the chamber in a plane perpendicular to the drawing plane a fast-load-lock-entry and the preparation and analysis tools are mounted. The system currently allows for sputter cleaning, Auger electron spectroscopy (AES) and evaporation from two metal sources, electron beam evaporator or Knudsen cell. An

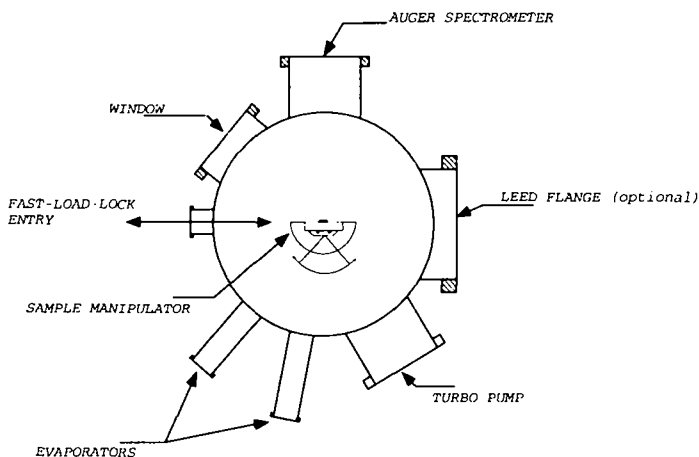


Figure 3.9: Vertical section of the UHV-chamber: Sample preparation stage.

additional flange for a low energy electron diffraction (LEED) system is also available. Refer to Figure 3.9 to see the exact arrangement.

Just to the right of this plane a pyramid-like bulge with a CF35-flange is located. This flange accommodates a “wobble-stick” which is used to transfer the sample from the manipulator into the STM in the center of the cryostat on the right hand side of the chamber. A more detailed description of the cryostat and of the sample transfer system will be given in the following sections 3.4 and 3.6, respectively.

All experiments including the *in situ* sample preparation were carried out in ultra-high-vacuum. The system is pumped through a turbomolecular, ion, and a titanium sublimation pump. A sketch of the complete system is shown in Figure 3.10. The achieved base pressures are 3×10^{-10} mbar at a cryostat temperature of 300 K, 2×10^{-10} mbar at 77 K, and 8×10^{-11} at 4 K.

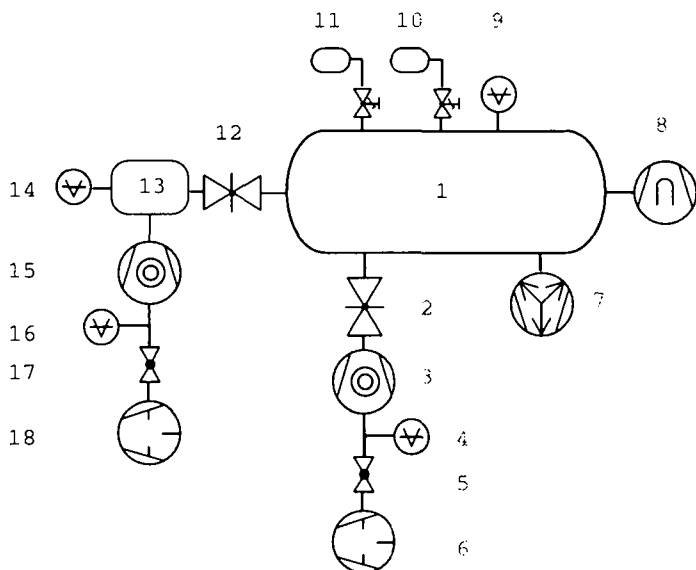


Figure 3.10: Sketch of the UHV-system. 1: UHV-chamber; 2: Gate valve; 3: Turbomolecular pump (350 l/s); 4: Pirani gauge; 5: Seal valve; 6: Rotary pump; 7: Ion pump; 8: Titanium sublimation pump; 9: Ionization gauge; 10, 11: Gas inlet; 12: Gate valve; 13: load-lock; 14: Cold cathode gauge; 15: Turbomolecular pump (50 l/s); 16: Pirani gauge; 17: Seal valve; 18: Rotary pump.

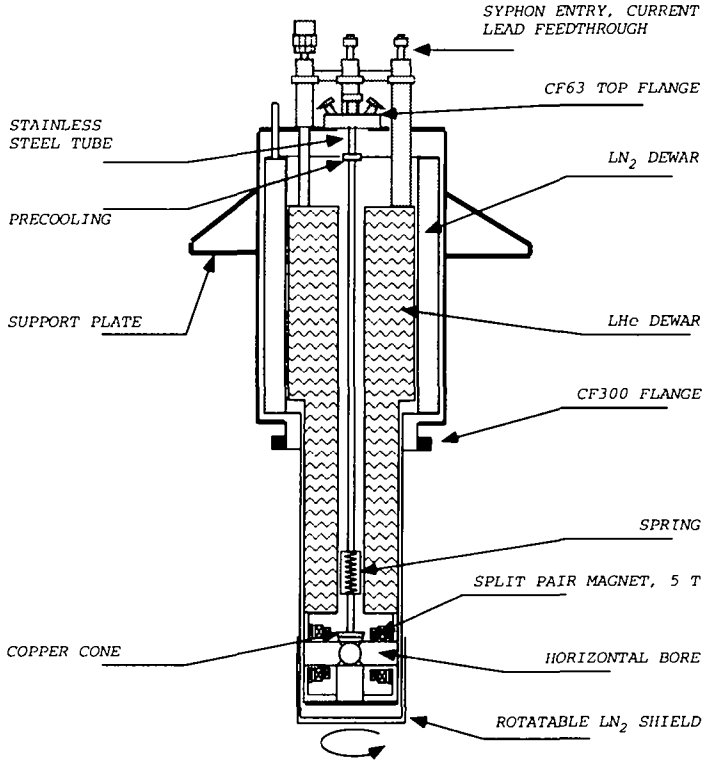


Figure 3.11: Vertical section of the cryostat.

3.4 The cryostat

Figure 3.11 shows a vertical cut through the cryostat [33]. Since vibration induced by boiling refrigerants can more easily be omitted in a bath cryostat than in continuous-flow cryostats the former design has been chosen. Besides the cooling of the superconducting magnet requires this cooling scheme as well.

The drawing shows two out of three triangular shaped support plates that have been welded to the exterior of the cryostat. They are used as support for the pneumatic dampers between cryostat and UHV-chamber. The complete inner part is surrounded by a liquid nitrogen (LN_2) dewar and a cylindrical

copper extension which shields the lower cryostat part. One step further to the center the liquid helium (*LHe*) dewar is depicted. It has a volume of 42 l and is equipped with a superconducting helium level meter. At its bottom the coils of a 5 T superconducting magnet with vertical field direction have been drawn (the cross-marked rectangles). The magnet is built in a so-called split pair arrangement. This offers the possibility to have two horizontal and one vertical bore of 50 mm diameter through the magnet while keeping the field homogeneity in a central cube ($V = 1 \text{ cm}^3$) better than 1 %. The horizontal bores are used for the sample transfer into the STM and for optical access to the microscope allowing to observe the sample transfer to the STM or to implement optical measurements inside the cryostat at low temperature. During the measurement the bores can be closed by a rotatable copper shield cooled from the LN_2 dewar to about 100 K. This measure reduces boiling of the *LHe*, accelerates temperature equilibration and eliminates thermal drift. Due to small heat capacity at low temperature the 300 K radiation through the bores (though they form a rather small solid angle with respect to the total $4\pi^2$) would otherwise increase the temperature of the sample to about 9 K. Nevertheless the heat load elicited by the shields at 100 K has also been taken into consideration. As in our experiments we do not use two out of the four bores, we closed them by an aluminum plug. A third one used only for the observation of the sample transfer has been closed by an infrared absorbing sapphire window. Furthermore it is preferable to chose an STM design that by itself screens the piezoceramics and other parts responsible for thermal drift from residual radiation (see section 3.5.1).

From the CF63 flange in the center of the top plate a stainless steel tube is running down to the magnet. The tube is thermally anchored at the walls of the LN_2 dewar in order to decrease the temperature gradient and the *LHe* consumption. A copper cone welded to the end of the tube is pressed into its counterpart at the top of the magnet by a spring loaded mechanism. As we will see in the following section the STM is fixed at this copper cone which is supposed to be at 4.2 K. All five CF16 electrical feedthroughs for the STM and one CF16 for the temperature sensor are installed on the CF63 top flange. All wires are special cryogenic wires [34] with low heat conductivity made from copper-bronze and stainless steel, respectively. They are thermally anchored by winding them several times around the vertical tube and around special heat sinks which are cooled to 77 K. Finally, they are glued to the copper cone with thermally conducting low temperature epoxy [35].

The LN_2 and the *LHe* dewars are connected to the top plate of the cryostat by three stainless steel tubes each. They serve as exhaust for the evapo-

rating liquids. Some of them are additionally used to insert the level probes, the helium transfer tube or as a feedthrough for the 120 A current leads of the magnet. When measuring at low temperature boiling of the LN_2 can cause mechanical excitations which can disturb the tunneling current or even provoke tip crashes. It is therefore necessary to pump on the nitrogen dewar in order to solidify the liquid and to eliminate any bubbling. The interior dewar if filled either with nitrogen or helium does not require pumping because of the shielding established by the exterior dewar. If, however, also boiling of LHe caused problems it would be possible to pump on the helium dewar as well. Decreasing the pressure to less than 40 mbar induces a phase transition in LHe which becomes superfluid. The absence of viscosity in the liquid then eliminates bubbling in the fluid.

3.5 The low temperature STM

In this section a description of the low temperature STM (LTSTM) along with a detailed characterization of its properties will be given.

3.5.1 Description of the design

Figure 3.12 shows a sketch of the STM. In principle the design can be understood as a combination of a scan head as in the nanoscope design with the approach mechanism of the Besocke [36] microscope. The aim for this is to combine the stability of the former type with the flexibility of the latter.

In the center of the drawing the scan piezo with the tip pointing to the bottom is shown. It is glued to a molybdenum disk with the well known triple helix on its under-side. The disk resides on three sapphire balls at the end of the exterior piezos. Those are glued to the body of the microscope which is a kind of cylindrical pot made from copper. The body has been gold plated in order to prevent it from oxidizing and to establish a good thermal contact to the copper cone of the cryostat (see section 3.4). A temperature sensor is glued to the bottom of the microscope.³ Control measurements proved the absence of any temperature gradient between copper cone and microscope body. Underneath the piezos a horizontal slit serves as a port for the sample holder. When the scan disk has been retracted by rotating it to the summit of the ramps by a “stick-and-slip” movement the sample can be transferred to or from the microscope. Pushing the sample holder into the microscope causes three conical “Teflon” plugs to be retracted. Copper-bronze springs are fixed to these plugs pressing the sample to the top against a polished surface. In this way the distance between the sample and the tip is always well defined. A similar spring-loaded mechanism is used to establish the electrical contact to the sample which is isolated from the sample holder by sapphire rings (see section 3.6). In the direction perpendicular to the transfer direction the microscope cylinder has two tiny openings of $5 \times 5 \text{ mm}^2$ one on each side. They allow optical access to the microscope in order to observe the sample transfer by a CCD-camera (charged-coupled-device). In the future they could also be used for optical experiments in grazing incidence geometry.

Another sensitive part of the LT-STM is a proper electrical connection of the piezos and the tunneling tip. This has mainly two reasons:

1. Since space is very limited in the cryostat one has to consider the

³This is a commercial thin film sensor with extreme low power consumption and independence of magnetic fields [34].

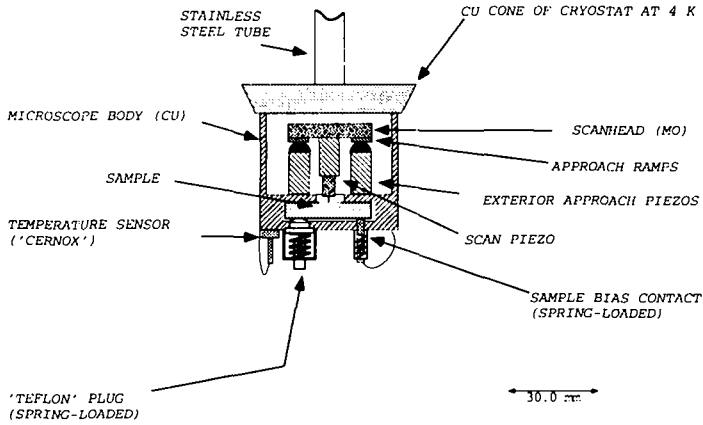


Figure 3.12: Schematics of the low temperature STM.

forces of the wires onto the moving parts of the microscope. Experience shows that they can hinder a proper operation of the "stick-and-slip" movement.

2. As all wires are connected to electrical circuits working at 300 K they need to be thermally anchored. Otherwise they could prevent successful cooling of the STM and the sample and lead to high drift.

Regarding 1: As compared to the standard beetle type microscope [28] the moving part of the present design has twelve wires (used for the exterior approach piezos) less. This already reduces the corresponding forces considerably. Additionally, the seven residual wires are connected to the disk at a small distance from its center hence applying only a small torque to it. However, since the distance from the top of the scan disk to the bottom of the copper cone is only three millimeters it is impossible to pass the wires directly through holes in the copper plane. The flexible length would be too short. The problem can be solved by passing the wires over a distance of about 20 mm through the vertical stainless steel tube in the center of the cryostat (see section 3.4). In order to keep them in an approximately constant distance from each other and to shield the tunneling current from crosstalk from the scan electrode wires, all of them are fed through a coaxial aluminum piece which has been inserted into the tube. The aluminum insert (Figure 3.13) has been anodized because mechanical contact of the wires

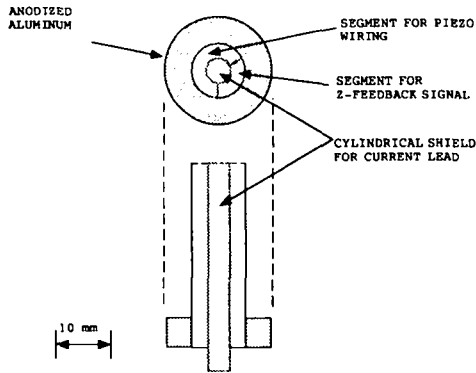


Figure 3.13: Anodized aluminum insert. Bottom and side view.

with this part cannot be excluded. A failure of the “Capton” wire insulation could in such a case produce short-circuits.

Regarding 2: The wires running down the vertical tube of the cryostat are made from thermally low conducting materials. Copper-bronze has been chosen for the connections of the piezo electrodes and stainless steel for the miniature coaxial cables conducting the tunneling current, the sample bias, and the z -feedback signal. All of them have been thermally anchored first by winding them several times around the vertical tube and special heat sinks at liquid nitrogen temperature (see section 3.4). On the top of the copper cone the wires are finally wound around and glued to small copper cylinders by a special thermally conducting low temperature epoxy. Since a proper thermal anchoring of the coaxial cables is more difficult to obtain special copper plugs were glued onto the cone. This is especially important because heat could otherwise be conducted directly to the tunneling tip where it would cause severe drift problems due to the small heat capacity. A sketch of these plugs is shown in Figure 3.14. In order to facilitate the dismantling of the STM the other wires are as well joined to the microscope by tiny gold plated connectors. The connections to the interior scan piezos are then continued with copper wires as their good thermal conductivity is helpful in cooling the scan head down to low temperature. Otherwise it would be thermally contacted only by the point contacts between the three sapphire balls and the approach ramps.

A final heat source to be considered is thermal radiation from an environ-

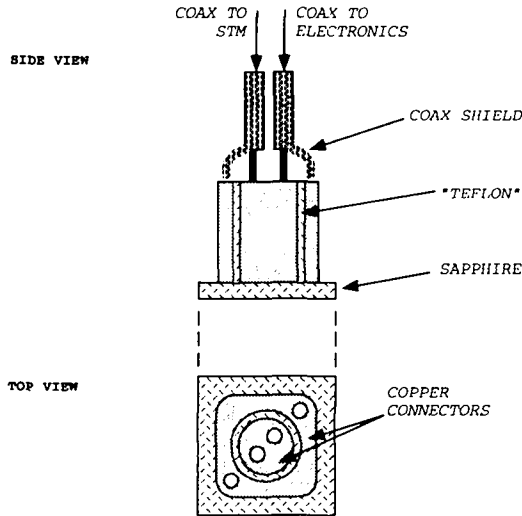


Figure 3.14: Thermal anchoring of coaxial cables. These plugs are glued onto the copper cone as depicted in Figure 3.12. The sapphire is used as electrical isolation.

ment at higher temperatures than the microscope. The horizontal bores of the cryostat constitute such a source as the shielding attains temperatures of approximately 100 K when the exterior dewar is filled with liquid nitrogen. As has been mentioned in section 3.4 all unemployed bores are hence either completely closed or a sapphire window has been inserted into the bore serving only as optical access. Besides the two openings in the cylindrical STM body the interior part of the STM with the piezo tubes, the tip, and the sample is completely shielded by the walls of the body itself. If, however, it was necessary, one could close the small openings by sapphire windows as well.

In the following paragraphs I will shortly line out why the above described design has been given preference over other currently used designs.

A first possibility is to build a microscope similar to the original Besocke design [36]. This concept has been adopted by Rossel and coworkers [37, 38], Stranick and Weiss [39, 40], Henderson et al. [41], as well as by Meyer [42]. Since the microscope can in principle be fixed tightly to the cryostat its thermal anchoring can be very good. Problems with forces from the wires can in this manner be omitted as well. On the contrary, it is more difficult to

realize a good thermal and electrical sample contact. Contacting it solely via the three sapphire balls or alternatively with electrically conducting metal spheres is not very convenient as it would take a long time to cool the sample. To get into thermal equilibrium with the cryostat any heat radiation onto the sample would be unacceptable. Finally, the Besocke design in conjunction with a sample transfer system requires some kind of additional sample approach mechanism because transferring the sample simply by a wobble stick directly onto the piezos and even more difficult to remove it from there, would probably not be successful.

Another microscope type to be considered is derived from the Besocke's design by turning it upside down in the sense that the microscope is the moving part and the sample is fixed. This version is now often used in variable temperature experiments [29, 43] because of its inherent temperature compensation and the possibility to combine it with a sample heater, continuous-flow cryostat and other surface analysis tools. This approach could solve the problem of slow temperature equilibration by fixing the sample tightly to the cryostat in a way similar to the one depicted in Figure 3.12. The microscope itself would not require a very good thermal contact as it is kept always at low temperature and as it could be shielded additionally. Likewise a mechanical manipulator used to put the scan head onto the ramps could be avoided simply by machining the ramps into the bottom of the cylinder forming the heat shield. However, the limited space in the cryostat makes it impossible to apply this concept to our case. Due to the requirement to keep the sample in the center of the magnet coils where the field is homogeneous the space between the top of the STM and the bottom of the copper cone above would be reduced to 3 mm. Being consequently forced to pass the 21 STM wires through the vertical tube in the center of the cryostat we face the problem that the inner diameter of 10 mm of this tube is too small to avoid the risk of crosstalk, short-circuits or to exclude a failure of the "stick-slip" movement.

The actually chosen design tries to take advantage from both of the two described possibilities and seeks to avoid some of their disadvantages.

The mechanical stability of the microscope should be as good as in the original Besocke design and better as compared to the beetle. This is because it has a very low center of mass with respect to the supporting sapphire balls. The distance of the center of mass from the plane defined by the summits of the balls is approximately 2 mm. For the beetle type the corresponding value depends on the length of the piezos and the weight of the STM disk (≈ 10 mm). Hence the new design allows to increase the weight of the disk resulting in an improved contact between the sapphire balls and the scan

head. This is realized by increasing its dimensions and machining it from molybdenum. The scan head in Figure 3.12 weights 37 g whereas a similar disk made from aluminum would weight only 10 g. As has been mentioned in section 3.1 also Behler et al. [29] propose in a recent paper that the quality of the contact can be improved by increasing the weight of the scan head. In the next section 3.5.2 we will see if this measure really has an influence on the eigenfrequencies of the microscope.

To summarize this section, I will list at the end of this section the principle properties of the low temperature STM:

- Low center of mass of the moving part of the STM. Increased weight of the scan head in the purpose to improve the mechanical support. Both properties should result in a higher mechanical stability as compared to the standard beetle type microscope.
- Inherent thermal shielding of the piezos, the tunneling tip, and the sample by the microscope body. This is especially important since the temperature compensation of the Besocke microscope has partially been lost by thermally anchoring the exterior piezos at different parts than the interior one.
- Spring-loaded sample slit providing a good thermal contact reducing the cooling time of the sample.
- Optical access to the microscope and the tip-sample region. In this way the sample transfer can be observed and light can be coupled into the tunneling junction.

3.5.2 Characterization of the STM

In the first section of this chapter the tunneling microscope has been modeled as a simple one dimensional oscillator with a damping constant c . In reality the microscope forms a three dimensional body with six internal degrees of freedom that could be excited to vibrations. All of them can cause a relative movement of the scan head with respect to the microscope cylinder. The mechanically weakest part in the design is the link between the scan head and the cylinder established by the piezo tubes. It is consequently allowed to neglect the elasticity of the disk and the cylinder. With the further assumption of zero mass of the tubes the microscope can be treated as a three dimensional harmonic oscillator rather than a three dimensional solid. The corresponding spring constants k and eigenfrequencies have been

Material	f_H [kHz]	f_R [kHz]	f_V [kHz]
Aluminum	4.4	4.7	19.1
Molybdenum	2.3	2.5	9.9

Table 3.2: Calculated eigenfrequencies of the LTSTM depending on disk material.

calculated by Behler et al. [29, 44]. For L being the length of the piezo tube, D and d the outer and inner diameter, and E Young's modulus, respectively, one obtains:

$$k_{\perp} = \frac{3\pi}{64} E \frac{D^4 - d^4}{L^3}$$

for the bending motion, and

$$k_{\parallel} = \frac{\pi}{4} E \frac{D^2 - d^2}{L}$$

for the stretching motion of one piezo.

The related frequencies for the beetle type geometry and the present LTSTM are identical because the contacts between the sapphire balls and the ramps are assumed to be rigid. One gets [29]:

$$f_H = \frac{1}{2\pi} \sqrt{\frac{3k_{\perp}}{M}},$$

for a horizontal displacement of the disk with respect to the cylinder and

$$f_V = \frac{1}{2\pi} \sqrt{\frac{3k_{\parallel}}{M}}$$

for the vertical direction. By taking account of the radius of the scan head r_1 and the distance of the exterior piezos from the vertical STM axis r_2 , one obtains

$$f_R = \sqrt{2} \frac{r_2}{r_1} f_H,$$

for the rotational vibration mode of the STM.

In Table 3.2 the corresponding frequencies of an STM with the dimensions of our LTSTM have been listed for a scan disk either made from aluminum or molybdenum.

Obviously, the situation is more favorable in the case of the light aluminum. However, the frequencies scale only with the square root of the masses. Therefore they decrease only by a factor smaller than two when replacing aluminum by molybdenum as disk material. Since the performance of the beetle type microscope is often limited by the above described "rattling"

motion of the scan head with respect to the sapphire balls (section 3.1) it is reasonable to replace the often used aluminum by molybdenum for the scan head.

It is possible to compare the theoretical estimations as listed in table 3.2 with experimental values obtained in using the STM as an accelerometer. By following the scheme introduced by Jericho et al. [45] we applied a sinusoidal signal to the $+x$ -electrode of the scan piezo and measured the response signal at the x - and y -electrode of an exterior piezo. The obtained data is represented in Figure 3.15 and 3.16. For comparison the frequencies from the aforementioned estimations are shown as well.

In Figure 3.15 the response spectra after excitation in the frequency range between 600 Hz and 7 kHz is shown. Curve I and II represent response spectra taken at 77 K at exterior piezo electrodes with perpendicular directions to each other. Both curves show several resonances between 2.3 kHz and 2.8 kHz. Note that in distinction to the beetle type the rotational angle between scan piezo and the exterior piezos depends on the actual position of the scan head. The fact that the relative amplitudes of the two spectra are similar might consequently be due to a excitation direction at 45 degree between the perpendicular directions of detection. This would happen when the interior piezo is rotated coincidentally by 45 degree with respect to the exteriors. Since the frequencies of the horizontal and the rotational vibration modes are close to each other we cannot attribute the measured resonances unambiguously to one of the modes. However, the good correspondence between the spectra and the theoretical values in table 3.2 suggests that the resonances frequencies have been correctly estimated by the above formula. The third spectra in Figure 3.15 represents a measurement performed after a macroscopic change of approximately 90 degree of the scan head position. Obviously, the relative amplitudes of the resonances have changed. The modified excitation direction can account for this effect.

Figure 3.16 shows a respective response spectra in the frequency range between 5 and 20 kHz. The resonance around 11 kHz can be attributed to the vertical vibration mode of the scan head. The correspondence with the numerical estimation is quite satisfactory. Such high eigenfrequencies are usually not very important as the related vibration damping is very good in this frequency range.

The most disturbing and hence most important resonances are, however, observed at frequencies between 1.2 and 1.8 kHz (see Figure 3.15). Upon changing the scan head position the form and exact position of the resonances changes. The most pronounced resonance at 1.8 kHz shifts by 200 Hz and

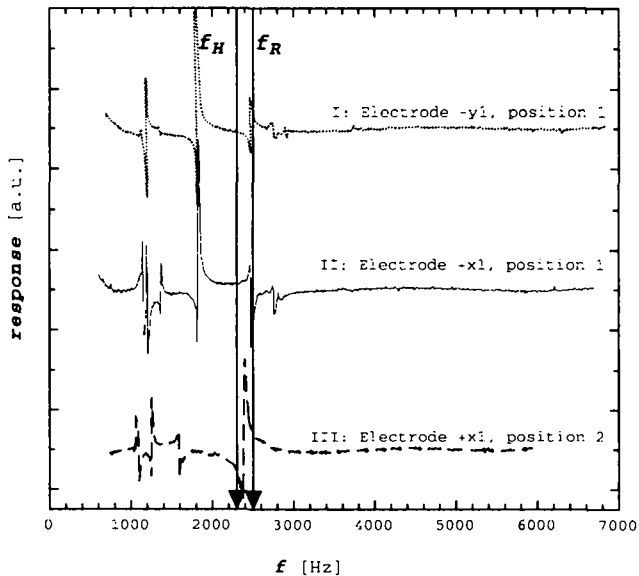


Figure 3.15: Response spectra from exterior piezo electrodes on excitation at the interior piezo. Curve I and II are taken on perpendicular electrodes while the third curve has been taken after a macroscopic change of the scan head position. f_H and f_R are numerical estimations described in the text. Curves are shifted for clarity.

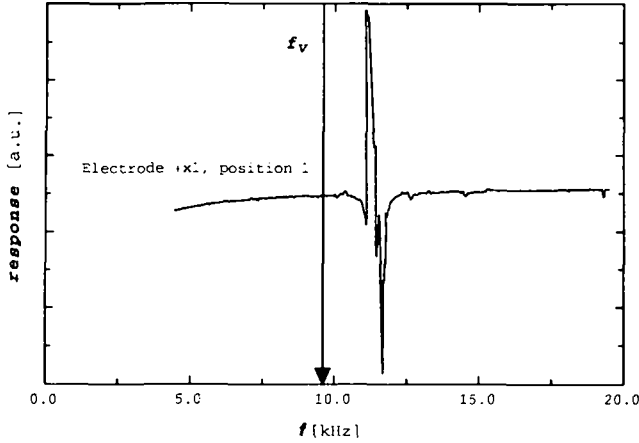


Figure 3.16: Response spectra from exterior piezo electrode x_1 upon excitation at the interior piezo.

changes drastically its amplitude. Behler et al. [29] attributed these modes to a “rattling” motion of the scan head with respect to the sapphire balls. Since their frequencies are lower than for the interior bending and stretching modes of the STM they are the first modes that are excited during tunneling measurements. They therefore constitute the limiting factor of several STM properties such as maximum scan speed and maximum gain of the feedback loop.

Spectra taken at frequencies smaller than 1 kHz did not show any resonances. This is a considerable improvement of the standard beetle type microscope where the “rattling” vibrations are generally found at frequencies between 500 and 1.7 kHz [29, 46]. As has been described in section 3.1 the higher weight of the scan head establishes a better contact with the sapphire balls and can hence account for the increase of the lowest eigenfrequencies of the scan head. As the “rattling” induces vibrations at frequencies still lower than the horizontal bending mode of the STM one could try to increase the scan head weight even further. Yet one has to consider a simultaneous decrease of the horizontal and rotational frequencies. Increasing the weight will hence approach the frequencies of the “rattling” and the bending motion resulting in a common value that will be situated between the present values.

We can use the above measurements to estimate the response of the LT-

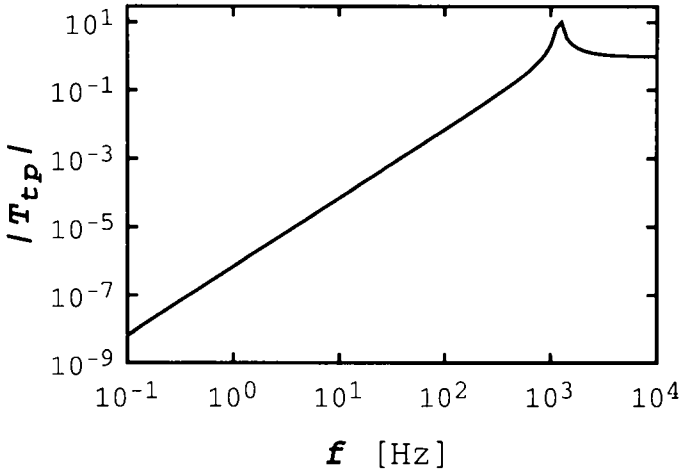


Figure 3.17: Transfer function of the tunneling gap.

STM to external vibrations. For this purpose we again consider it as a one dimensional harmonic oscillator with a lowest eigenfrequency at 1.2 kHz (Figure 3.15). Since the mass of the scan head is known the corresponding spring constant can be calculated by $k = 4\pi^2mf^2$. A value for the damping constant can be calculated from the typical Q factor of an STM [47]. With these values the transfer function of the tunneling gap can be calculated. The resulting curve is plotted in Figure 3.17. The curve increases at low frequencies with 40 dB per decade (as in Figure 3.2) and shows the lowest resonance of the microscope at 1.2 kHz.

To obtain the response of the tunneling gap to exterior building vibrations the transfer function has to be multiplied with the transfer function of the vibration isolation stage in Figure 3.8. The resulting overall response to building vibrations is shown in Figure 3.18. The damping is always—even in the resonances—better than 10^{-5} . Above 10 Hz the damping increases by ≈ 60 dB per decade and attains 10^{-15} at the first resonance of the microscope. From this theoretical point of view it is very improbable that building vibrations excite resonances of the STM. However, the calculation gives only a rough estimate since many approximations and simplifications have been made.

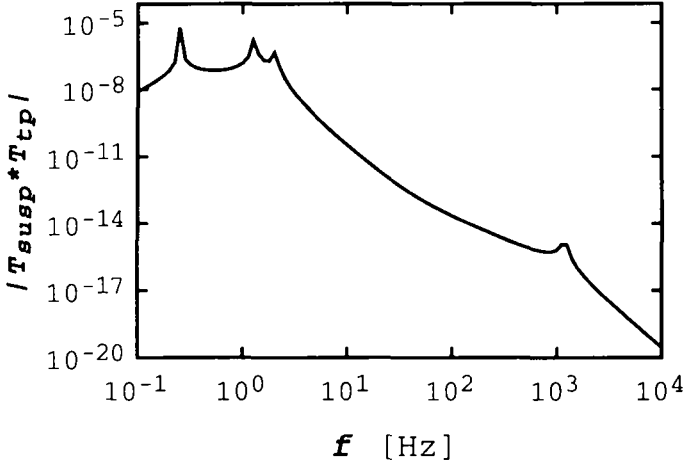


Figure 3.18: Response of the tunneling gap to building vibrations.

The response of the microscope to acoustic noise has to be considered differently. Although the sound insulation of the cubicle could be measured it is difficult to estimate noise pick-up by the UHV-chamber and the cryostat and even more to translate such data into mechanical vibrations of the STM-support. Anyhow, it is obvious that the stiff link between the cryostat will lead to a high sensitivity to acoustic noise. Hence all noise sources inside the cubicle have to be eliminated during measurements.

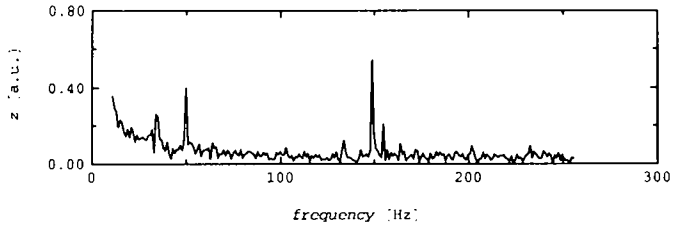
The modelisation of the tunneling gap by coupled harmonic oscillators leads only to a rough approximation of the real response function. However, it is particularly useful in order to determine the different vibration modes and consequently, the way how one should reduce their excitation. The most significant value that can be measured in order to characterize the vibrational noise transmitted into the tunneling gap is to carry out a frequency analysis of the feedback signal z . For this purpose the tip has to be kept at a constant lateral position and the feedback signal as a function of time $z(t)$ has to be measured. A Fourier transformation of the experimental values then leads to the relevant noise spectrum of the microscope. Such an analysis is shown in Figures 3.19 (a)-(c). The otherwise flat low frequency spectrum in (a) has resonances mainly at 50 Hz and 150 Hz. These frequencies coincide with the frequency of the mains and its second harmonic and can consequently

be assigned to electrical coupling transmitted by the power supply. Their amplitude is higher than any other mechanical resonance.

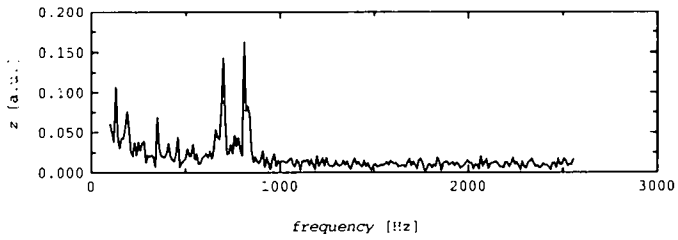
The spectra shown in (b) and (c) show several resonance peaks that we attribute to the mechanical eigenmodes of the STM. With respect to the results shown in Figure 3.15 and 3.16 all frequencies have shifted systematically to lower frequencies. It seems difficult to find a one-to-one correspondence between the resonances shown in Figure 3.19 and the eigenmodes of the STM. The spectrum in (b) only suggest that the peaks between 700 Hz and 900 Hz are caused by the “rattling” motion of the scan head or by the horizontal eigenmode of the microscope. The rotational mode should accordingly be the origin of the resonances at 2200 Hz or 2900 Hz. However, these assignments are only speculative. On the contrary, the peak at about 7700 Hz can be ascribed to the vertical vibration of the scan head with respect to the sample. Since the feedback signal is extremely sensitive to this motion the amplitude of this peak is higher as compared to other mechanical vibration modes between 2000 and 9000 Hz.

The amplitudes in Figure 3.19 are shown in arbitrary units and it is not possible to estimate the importance of the noise level from these spectra. From the topographic linescan in Figure 3.20 it becomes clear that the residual noise in the feedback signal $z(t)$ is very low. The cross-section has been taken along the horizontal direction of a topographic image of the Ag(111) surface. This is also the actual scan direction of the tip. The low-frequency modulation ($\lambda = 2.2 \text{ \AA}$) is due to atomic rows of the sample. The noise level that can be extracted from the linescan is approximately $4/1000 \text{ \AA}$. Images of metal surfaces with atomic resolution should thus be obtained routinely at low temperatures. In conjunction with the very low drift at 5 K the LTSTM is therefore suitable for atom manipulation experiments and high resolution tunneling spectroscopy. In chapter 4 measurements on the Au(110) surface will be used in order to characterize the behavior of the STM at temperatures between 300 K and 5 K.

a)



b)



c)

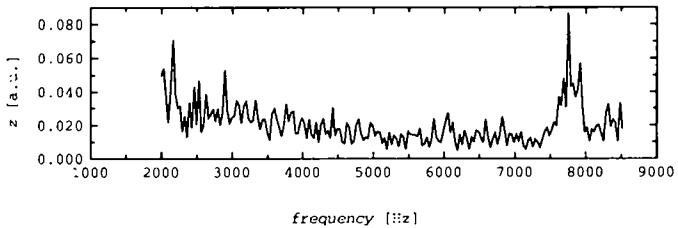


Figure 3.19: Measured frequency spectra of the feedback signal z . a) Electronic noise at 50 and 150 Hz. b) and c) Mechanical resonances of the STM between 700 Hz and 8 kHz. Note the relative scale of the spectra.

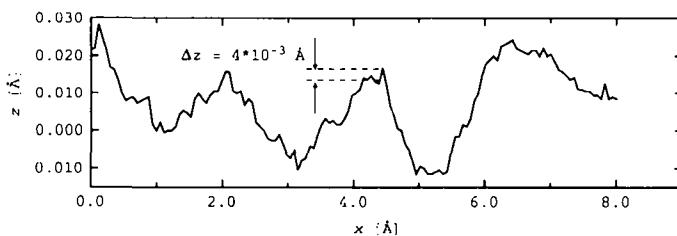


Figure 3.20: Horizontal linescan of a topographic image of a Ag(111) sample taken at 5 K. The low-frequency modulation ($\approx 2.2 \text{\AA}$) is due to the atomic corrugation (atomic rows are not parallel to the scan direction). The peak-to-peak noise level is $4/1000 \text{\AA}$.

3.6 The sample manipulation and transfer system

Low temperature scanning tunneling microscopes impose the difficulty that the sample surface preparation tools and the microscope have to be separated from each other. Therefore an in situ sample transfer system becomes necessary. Such a system must include the possibility to contact the sample electrically for the purpose of temperature measurements and e^- bombardment during preparation on the manipulator as well as for the sample bias potential during the tunneling measurements.

Additionally, a fast-load-lock is attached to the system that allows sample exchange without breaking the vacuum. Therefore the chamber is equipped with three sample manipulation tools: The variable temperature manipulator, the “wobble-stick” for sample transfer into the LTSTM and a linear magnetic drive at the load-lock.

3.6.1 The sample holder

To understand the sample transfer system it is best to start with an inspection of the sample holder. Molybdenum has been chosen as material because it is non-magnetic and resists high temperatures during sample preparation. Figure 3.21 shows a vertical cut. The hat-formed sample is electrically isolated from the holder by two thin sapphire rings. Sapphire as insulating material has been chosen because of its favorable temperature dependence of the thermal conductivity: At low temperatures the conductivity is by one order of magnitude higher as compared to ceramic aluminum oxide [48]. This allows a fast cooling of the sample. On the contrary, the thermal conductivity of sapphire becomes bad at high temperatures. Therefore heating of the sample by means of the electron beam heater on the variable temperature manipulator is facilitated because the heat loss to the surrounding sample holder is minimized.

On the left side of the drawing a horizontal bore in the sample holder is depicted. It is used for the sample transfer forks of the wobble stick and the fast-load-lock manipulator. The latter one, a simple magnetic linear drive, is employed to insert the sample through the lock into UHV. The bore can be retrieved in Figure 3.22 that shows a sketch of the top and bottom of the sample holder. In the top view one recognizes actually three bores for the sample transfer fork. The central one is part of a bayonet connection between the sample holder and the transfer manipulators. On the same

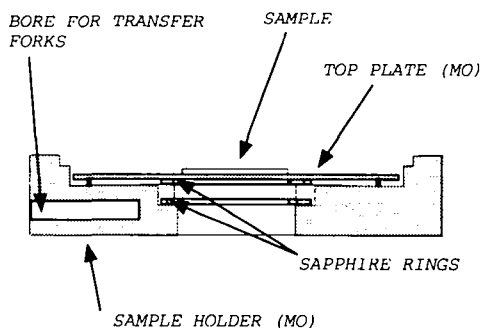


Figure 3.21: Vertical section of the sample holder.

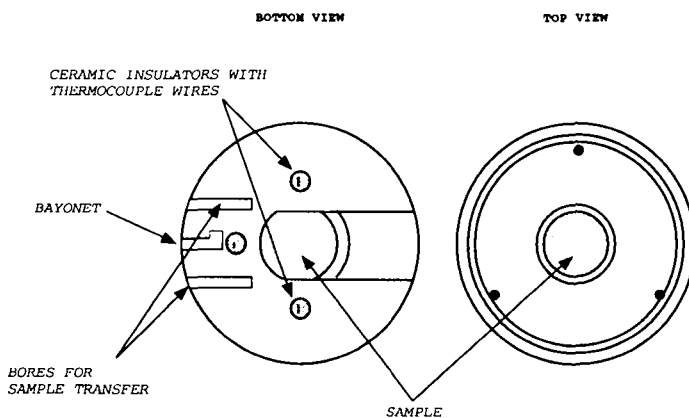


Figure 3.22: The sample holder with electrical contacts and bayonet joint.

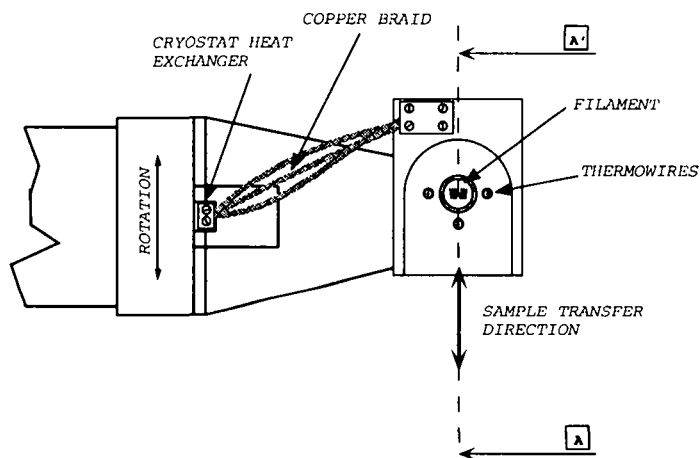
drawing three electrical contacts to the sample are visible that are connected to the sample. Two of them are used to measure the sample temperature (non-magnetic “Chromel-Constantan” thermocouple wires) and the last one to apply a potential to the sample. All wires are passed through ceramic (Al_2O_3) insulators.

3.6.2 The variable temperature manipulator

The electrical contact (thermocouples and sample bias) of the sample with the main sample manipulator is established by incorporating the wires into spring loaded ceramic tubes. Upon pushing the sample onto the manipulator the contacts are forced to retract. In the final position of the sample they are pressed against their counter contacts on the sample holder. Details can be seen in Figure 3.23. In the center of the manipulator end-plate the filament of the electron beam heater is shown.

The manipulator has three translational degrees of freedom and one rotational around the horizontal axis of the chamber. The rotational motion is transmitted from a CF16 feedthrough via a cardan joint(see Figure 3.24) to a rack-and-pinion mechanism at the head of the manipulator.

In the aim to control the growth of nanoscopic metal structures on the sample surface it might be necessary to cool the sample to low temperatures. Therefore the sample manipulator is equipped with a continuous-flow helium cryostat [49] that makes temperatures down to 40 K accessible.



SECTION A-A'

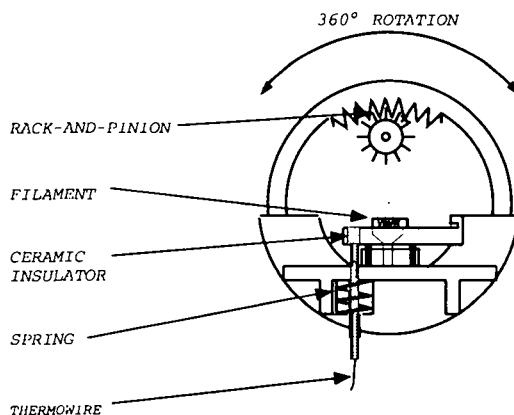


Figure 3.23: Head of the variable temperature manipulator with rack-and-pinion.

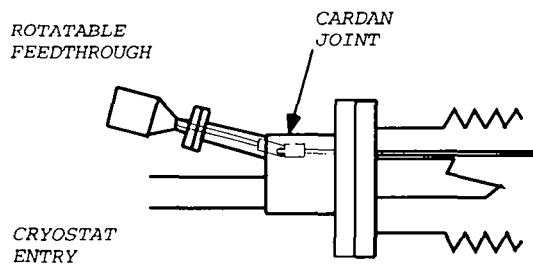


Figure 3.24: Cardan drive for rotational motion of sample manipulator.

3.7 Sample preparation and imaging conditions

3.7.1 Sample preparation

The Ag(111) single crystal was prepared *in situ* by repeated cycles of ten minutes Ar⁺-ion sputtering ($E = 800$ eV, $I_{\text{sputter}} = 5 * 10^{-6}$ A, $p_{\text{Argon}} = 5 * 10^{-6}$ mbar, and $T_{\text{sample}} = 300$ K) and subsequent annealing at 870 K during twenty minutes. During annealing of the sample the total pressure was $8 * 10^{-10}$ mbar. Prior to low temperature STM measurements the sample has been cooled on the variable temperature manipulator to temperatures $T \leq 150$ K.

Similar preparation cycles have been applied to the Au(110) sample. The ion energy in this case was $E = 600$ eV and the annealing temperature was 650 K.

Nickel and Niobium were evaporated from high purity sources (Ni 99.997 %, Nb 99.9 %) by means of a commercial electron beam evaporator. During deposition the chamber pressure stayed below $8 * 10^{-10}$ mbar. Deposition temperatures varied from 130 K to 300 K.

3.7.2 Imaging conditions

If not otherwise stated all images shown in the following chapters represent topographical images obtained in constant current mode with a commercial STM control system [50]. Besides a subtraction of a background and subsequent readjustment of the greyscale distribution no further image processing were applied to measurements if not otherwise indicated. The tunneling voltage U_S was always applied to the sample.

The spectroscopical dI/dV measurements presented in chapter 5 were acquired using lock-in detection. The tunneling voltage was modulated by 5 mV (peak-to-peak) at a frequency of 1.72 kHz and the lock-in signal was recorded at a time constant of 1 ms.

Chapter 4

STM calibration on Au(110)

In the aim to calibrate the microscope at all accessible operation temperatures and to characterize its performances in more detail I will now turn to measurements that were performed on a Au(110) surface. This sample is well suited for calibration purposes because firstly, the sample is simple to prepare, secondly, the resolution of the (1×2) -reconstruction is easy to obtain. Finally, since atomic resolution along the $\langle 1\bar{1}0 \rangle$ rows is very difficult to achieve one has the possibility to test the resolution performance of the microscope.

As it has been lined out in the introduction the main purpose of the present LTSTM will be to study physical properties of nanoscopic structures on the sample surface as a function of their size and shape. A second motivation why we chose the Au(110) sample is the anisotropy of this surface that might offer the possibility to tailor the shape of adislands that can be created by self-organized growth. Recently, Vieira and coworkers [51] reported on the observation of superconductivity of lead clusters deposited on a Au(111) surface. The authors claimed to have observed superconductivity even in particles that were smaller than the electron coherence length in bulk lead. By the choice of Au(110) one might be able to perform similar experiments with the additional possibility to grow *in situ* one or two dimensional particles by a proper choice of the preparation parameters. Preliminary experiments were carried out using niobium evaporated at low temperature onto the Au(110) surface.

4.1 The Au(110) surface

In the past the Au(110) surface has been studied by numerous techniques. In these studies the structure of the thermodynamically stable ground state

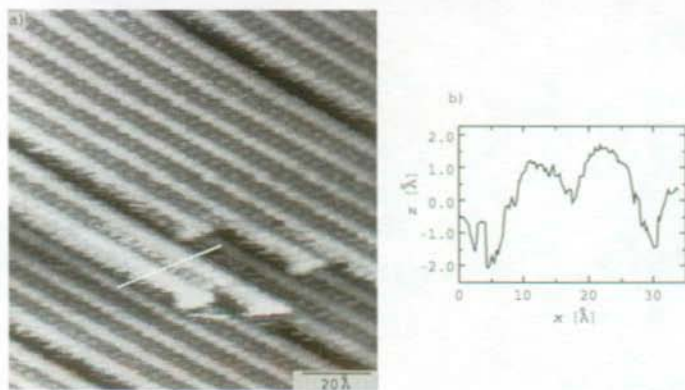


Figure 4.1: a) Au(110)(1×2) "missing row"-reconstruction imaged at 300 K. b) Line scan as indicated in (a).

has attracted the main interest. It is now consensus that the structure of the Au(110) surface in equilibrium is characterized by a (1×2)-reconstruction where every second $\langle 1\bar{1}0 \rangle$ row is missing. The reconstruction is consequently called "missing-row" reconstruction. In an early STM study Binnig et al. [52] pointed out that the reconstruction results from the formation of $\{111\}$ -facets by the remaining densely packed atom rows running along $\langle 1\bar{1}0 \rangle$. The micro-facetting lowers the total surface energy with respect to the unreconstructed surface even if one takes account for the increased effective surface area. First principles calculations by Ho and Bohnen [53] showed that the energy decrease is due to a decrease of the kinetic energy of delocalized electrons at the surface.

Figure 4.1 (a) shows an image of the atomically resolved clean Au(110) surface. The measurement has been carried out at 300 K. All terraces are generally dominated by the (1×2) "missing-row"-reconstruction. Only in some minor cases the surface exhibits a (1×3)-reconstruction that forms troughs of increased depth and width. The maxima appearing in the STM image in Figure 4.1 (a) inside the (1×2)-troughs are not due to individual atoms within the troughs. The model in figure 4.2 shows that the removal of a monatomic $\langle 1\bar{1}0 \rangle$ row leads to the exposure of in total three atomic rows underneath. From the geometry of the surface it becomes clear that one can expect to resolve either two or three atomic rows within the reconstruction troughs but not only one (since this would be the lowest row in the trough). The structure resolved between the reconstruction rows in Figure 4.1 (a) can

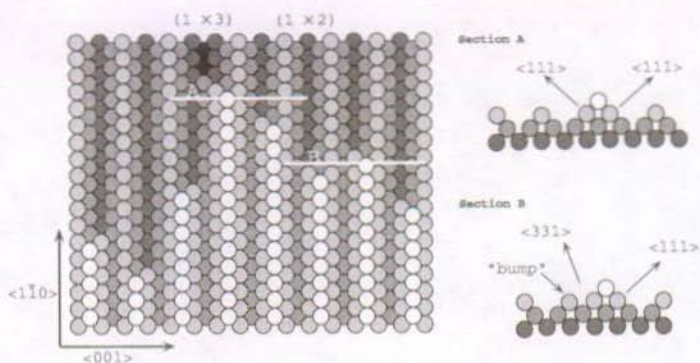


Figure 4.2: Model of the (1×2) "missing row"-reconstruction. The lowest terrace is partially (1×3) reconstructed. Section A and B indicate the topographic difference of $\{331\}$ and $\{111\}$ facets.

therefore be due to an electron density of states that does not follow the simple geometric picture or to a convolution of tip states with sample states that might smear out the image contrast.

The STM image in figure 4.1 (a) shows further characteristic properties of the Au(110) surface. Firstly, the morphology of $\langle 001 \rangle$ and $\langle 1\bar{1}0 \rangle$ steps is very different from each other. $\langle 1\bar{1}0 \rangle$ steps can run over several thousand Angstrom with a very low density of kinks. In contrast the surface usually does not form straight steps along $\langle 001 \rangle$. This difference can be assigned to the stabilization of $\langle 1\bar{1}0 \rangle$ steps by the formation of $\{111\}$ -micro-facets and the low interaction between neighboring $\langle 001 \rangle$ rows. Therefore the formation of straight $\langle 001 \rangle$ steps is much less favored. Secondly, when a terrace terminates on an underlying (1×3) -reconstruction then both $\langle 1\bar{1}0 \rangle$ -steps of the terrace form $\{111\}$ facets. If the underlying terrace is completely (1×2) reconstructed one of the steps forms a $\{331\}$ and the other one forms a $\{111\}$ facet. As Gritsch et al. [54] showed this leads to asymmetric terrace shapes since the $\{111\}$ stabilized step tends to be longer. The small terrace in the lower half of the image is an example of a terrace that terminates on a (1×3) -reconstruction. If the facets formed by the steps of this terrace were different the line scan in figure 4.1 (b) would reflect the asymmetry by an additional bump at the $\{331\}$ -facet.

Though the image in figure 4.1 (a) has been taken at room temperature it is generally easier to obtain atomic resolution at low temperatures because the tunneling tip is more stable and thermal drift is reduced to a minimum

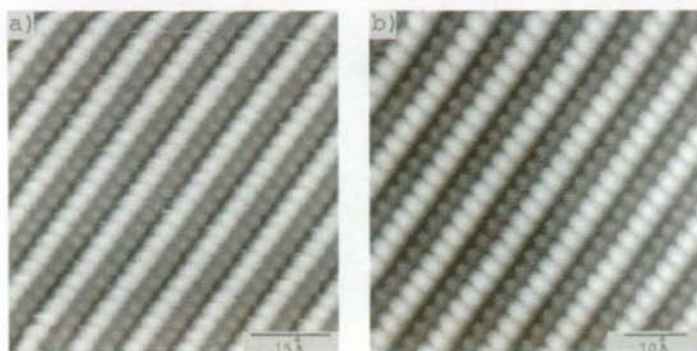


Figure 4.3: Atomic resolution images at 77 K (a) and 5 K (b).

Temperature [K]	Horizontal conversion [$\text{\AA}/\text{V}$]	Vertical conversion [$\text{\AA}/\text{V}$]
300	75.2	14.4
77	50.9	9.8
4	29.5	5.7

Table 4.1: Piezo conversion factors at different temperatures.

(see section 3.5.2). Furthermore decreasing the temperature causes the piezo conversion factors to decrease as well. They are therefore less sensitive to noise that is introduced by the STM control electronics. Depending on the piezo ceramic material the conversion factor can decrease by a factor of 8 when the STM is cooled from 300 K to 4 K. In order not to reduce the maximum scan area too much we chose a piezo ceramic [55] with a small sensitivity to temperature variations. In table 4.1 experimentally observed values are shown. At the highest scan voltage of ± 200 V a maximum scan range of 1180 nm is still achievable at 5 K (corresponding to a factor < 3 between the conversion factors at 300 and 4 K).

Figure 4.3 gives examples of experiments at 77 and 5 K, respectively. As in figure 4.1 the structure within the troughs cannot be attributed to individual atoms. Figure 4.4 demonstrates that the image contrast depends strongly on the tip properties. Now two of the three atomic rows in the troughs are atomically resolved, however, they appear asymmetric in contrast to their actual geometry.

The nucleation of single atoms on a sample surface into stable adislands depends both on the diffusion constant and on the sticking coefficient of dif-

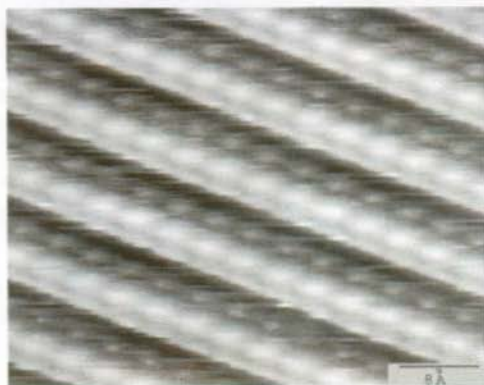


Figure 4.4: The (1×2) -reconstruction at 77 K. Individual atoms within the troughs are imaged.

fusing atoms that get into contact with the edge of an adsorbed island. Since on an anisotropic surface both properties (diffusion and sticking) become dependent on the direction relative to the surface symmetry directions, one might be able to grow one- or two- dimensional adislands simply by selecting appropriate evaporation parameters.

It is known from literature that the Au(110) surface as well exhibits anisotropic diffusion. Behm and coworker [56] studied the growth of Ni on the reconstructed surface. Experiments performed at room temperature showed the presence of monatomic Ni chains embedded in the (1×2) -reconstruction troughs. Recently, the same behavior was observed for submonolayer growth ($\Theta < 0.2$ ML) of Cu on Au(110) [57].

Following these examples first steps in the submonolayer growth of niobium on the Au(110) surface were studied. However, at temperatures between 130 K and 300 K niobium does not form monatomic chains. In figure 4.5 (a) the Au(110) surface after an evaporation of Nb at 130 K is shown. During the transfer of the sample to the LTSTM its temperature was not allowed to increase significantly.¹ When the precooled sample has been

¹The "wobble-stick" is not equipped with a separate cryostat. The sample temperature will therefore rise slightly during the transfer to the LTSTM. To minimize the increase of temperature, all parts of the "wobble-stick" that have a good thermal contact with the sample holder are designed to have a low heat capacity and are thermally isolated from the rest of the "wobble-stick". If this measure was not sufficient one could additionally precool the "wobble-stick" by pushing it into a horizontal bore of the cryostat or by putting it

transferred to the STM it reaches within about 30 min the temperature of the bath cryostat of 77 K or 4 K, respectively.

Figure 4.5 (a) shows small particles that are incorporated into the troughs of the Au(110)-(1 × 2)-reconstruction. Though atomic resolution on these clusters has not been achieved their shape indicates that they consist of two or three atoms. These atoms consist not necessarily of adsorbed Nb as exchange processes between Nb and Au atoms can take place. Such a behavior has been observed in the Ni/Au(110) system [56]. In order to identify the atoms residing in the troughs we consider their imaging height. From the line scan in Figure 4.5 (b) one can see that the clusters protrude from the summit of the reconstruction rows by 1.1 Å. Since for Au atoms one would not expect any protrusion we can conclude that the clusters are probably formed from evaporated niobium. Besides these clusters Figure 4.5 shows other modifications of the sample surface. Several gold atoms in the reconstruction rows have been replaced by atoms that appear with a different imaging height (indicated in the Figure by "A"). Furthermore the evaporation of niobium has led to point defects in several (1 × 2)-reconstruction rows where gold atoms have been ejected leaving monatomic vacancies behind (indicated by "B").

Keeping the sample at room temperature during evaporation while leaving all other parameters unchanged, results in important changes of the surface morphology that are presented in Figure 4.6 (a). Now Nb forms symmetrical clusters that are only partially embedded in the reconstruction troughs. Since they have moved slightly along the $\langle 001 \rangle$ direction each cluster now shades one maxima of the underlying reconstruction rows. This is confirmed by the line scan in Figure 4.6 (b) that shows a height of the clusters of 1.4 Å.

The point defects caused by monovacancies in the gold substrate have disappeared. Apparently, they can coalesce into monatomic vacancy chains in the rows or they cause locally a rearrangement of the topmost substrate layer. In consequence the (1 × 2)-reconstruction can either be changed into a (1 × 3)-reconstruction (e. g. at "A" in Figure 4.6 (a)) or the reconstruction can be lifted completely (e. g. at "B").

The preliminary experiments show that the growth of niobium on Au(110) establishes a process involving restructuring of the substrate even at low temperature. Especially, the modifications of the substrate by the atom exchange and the partial lifting of the surface reconstruction hinder a simple shape tailoring of adislands. Furthermore the contamination of Nb originating from the source (highest available purity is 99.9 %) and from chemical reactions with the residual gas atmosphere in the UHV-chamber cause severe prob-

into contact with the sample manipulator for several minutes.

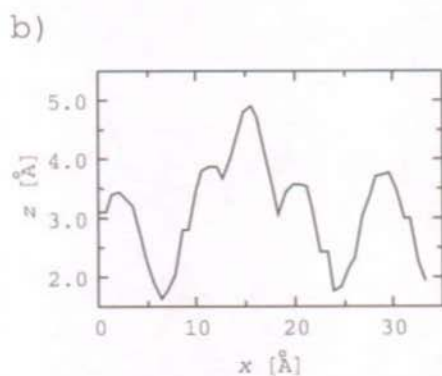
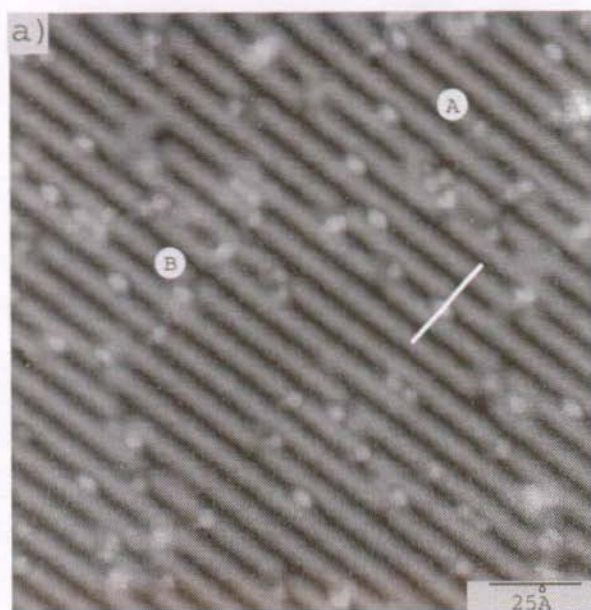


Figure 4.5: a) Nb islands grown on Au(110) at 130 K and imaged at 77 K. Nb forms small, slightly elongated clusters in the troughs of the (1×2) -reconstruction of the substrate. b) Line scan as indicated in (a).

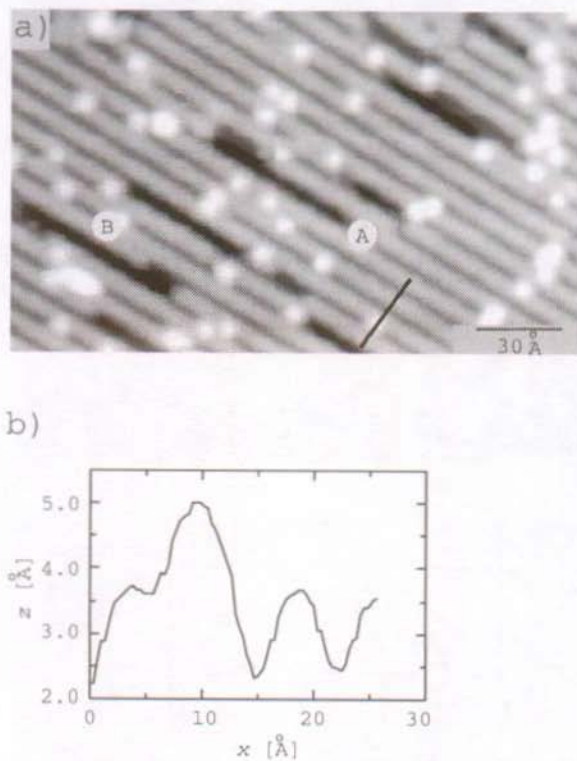


Figure 4.6: a) Nb islands grown on Au(110) at 300 K and imaged 77 K. Nb forms small, slightly elongated clusters in the troughs of the (1×2) -reconstruction of the substrate. b) Line scan as indicated in (a).

lems. The study of the superconductivity of mesoscopic Nb particles would require a better structural and chemical characterization of the sample than it has been possible for us to date. In particular to test our spectroscopical measurement scheme, it is necessary to be able to prepare a sample that is known to be superconducting or not. Therefore the Au(110) surface was only used to calibrate and characterize the LTSTM and the sample preparation tools.

Chapter 5

Surface States on Ag(111)

5.1 The surface state on Ag(111)

The property of the electrons in a solid to condense in collective and continuous energy bands was recognized in 1931 by Kronig and Penney who published a model in which the crystal lattice was represented by an infinite periodic chain of one-dimensional square potential wells. The periodicity of the potential causes the formation of continuous bands of allowed energies that are separated from each other by intervals of forbidden energy values where no physical solution of the Schrödinger equation exists. Wave functions in the forbidden energy range would diverge within the crystal and must therefore be excluded. Already in 1932 and 1939 Tamm [58] and Shockley [59] found an important modification when the infinite crystal is replaced by a semi-infinite one that is, a crystal with a surface. The authors showed that in this case a new type of states with energies within a band gap of the solid exist that are localized at the surface decaying exponentially into the bulk and the vacuum. Thereby a confined two dimensional electron gas is formed.

Especially, the noble metal (111) surfaces of copper, gold and silver are known to form surface states of an almost ideal two-dimensional (2D) free electron gas. The current understanding of these states is mostly due to photoemission studies which have been the standard technique of their investigation for over twenty years. By angle-resolved photoemission (ARUPS) experiments the electronic dispersion relation has been investigated as well as the interaction of surface states with bulk states and with contaminants. The first evidence of the surface state on Cu(111) was found in the experiments of Gartland and Slagsvold [60]. From the sharpness of a peak in the energy distribution spectra, its dependence on the angle of incidence and sensitivity to oxygen contamination the authors concluded on the observation of a

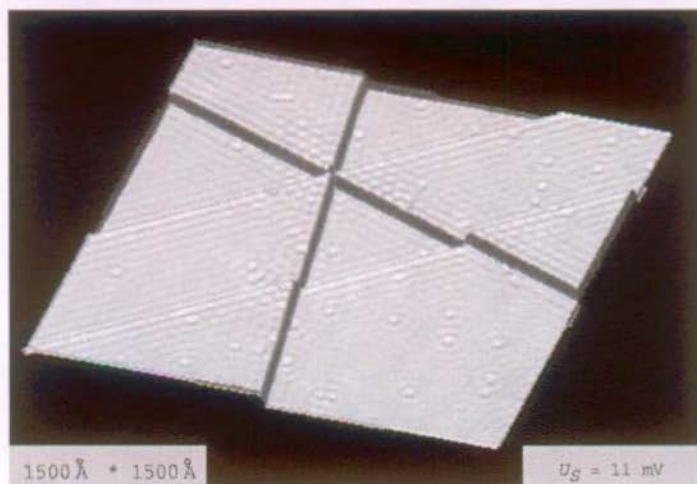


Figure 5.1: Three dimensional representation of the Ag(111) surface acquired at 5 K. The standing wave patterns are caused by scattering of the surface state electrons at step edges and impurities. (Low-pass filtered data)

electronic state localized at the surface.

Recent photoemission spectra [61] show that the onset energy of the surface state on the (111) surfaces of Cu, Au, and Ag is situated between -0.45 meV and the Fermi energy E_F when the temperature of the sample is smaller than 400 K. This energy range is easily accessible to tunneling spectroscopy. Along the lines described in chapter 2 it is therefore possible to determine the electron density contribution of the surface state by tunneling spectroscopy (see equation 2.12). Davis *et al.* were the first to employ this technique for the investigation of the surface state of Au(111) [62]. Direct observation of a standing wave pattern caused by scattering of the 2D electron gas off step edges and impurities was achieved for the first time by Hasegawa and Avouris on Cu(111) and Au(111) [63] and Crommie *et al.* [64], respectively. Until today several other studies have been reported both at room temperature and at low temperatures [65, 66, 67, 68, 69].

In the study by Li and coworkers the Ag(111) surface has been investigated at temperatures down to 5 K. The tunneling current spectra taken at 50 K showed the onset of the surface state 67 meV below Fermi. This is in good agreement with photoemission measurements where a value of 61 ± 5 meV was found.

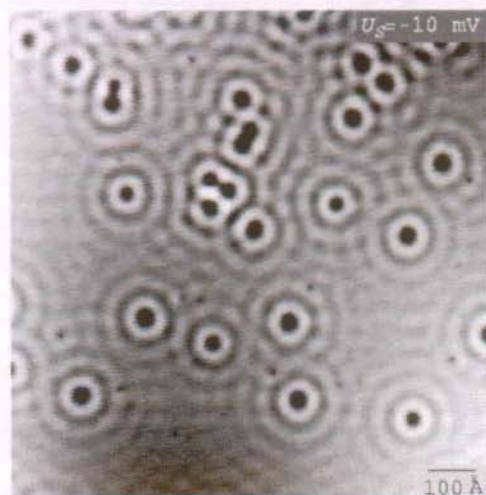


Figure 5.2: Scattering of the 2D-electron gas off point defects. The image has been taken at $T = 5$ K.

Since a considerable contribution of the surface state to tunneling current is found up to 100 mV above Fermi a measurement taken at a sample bias voltage $U_S = 11$ mV should reflect surface electronic properties caused by the surface state. Such an image is shown in Figure 5.1. From each of the step edges parallel plane waves are spreading out onto the terraces. Such waves are caused by a partial reflection of the surface state electrons at surface defects like step edges or point defects. While spreading out from the steps onto the terrace the waves decay. After about nine consecutive maxima no clear wave front can be identified any more. In the corner of a terrace where two step edges cross each other under an angle of 60° interference between the plane waves take place. This leads to the formation of a typical interference pattern with maxima and minima in the apparent surface height. The same behavior can also be observed between waves coming from point defects as scattering centers. An example is given in Figure 5.2.

Figure 5.3 gives a more detailed view of the scattering of electrons at a step edge. The atomically resolved hexagonal surface shows height modulations on both terraces which follow the shape of the step. On the right terrace the modulation is complicated by additional scattering at a small pit in the vicinity of the step.

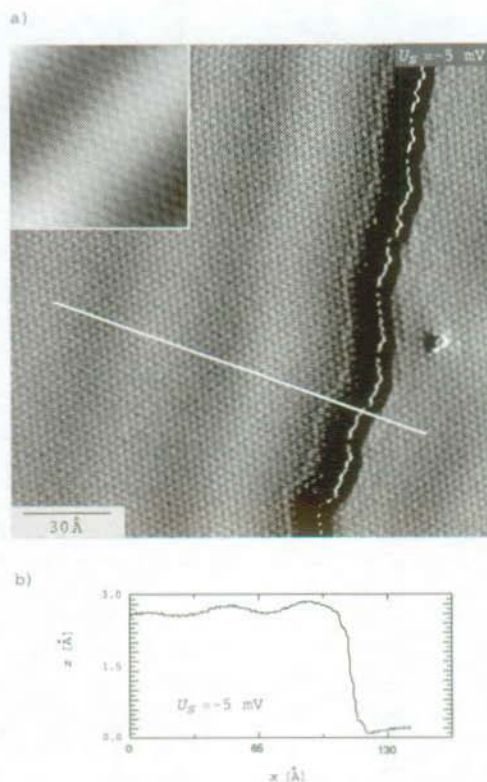


Figure 5.3: a) dz/dx -representation of the Ag(111) surface in the vicinity of a step. The inset shows a constant current image of an equivalent region on the surface. b) Line scan as indicated in (a). ($T = 5 \text{ K}$)

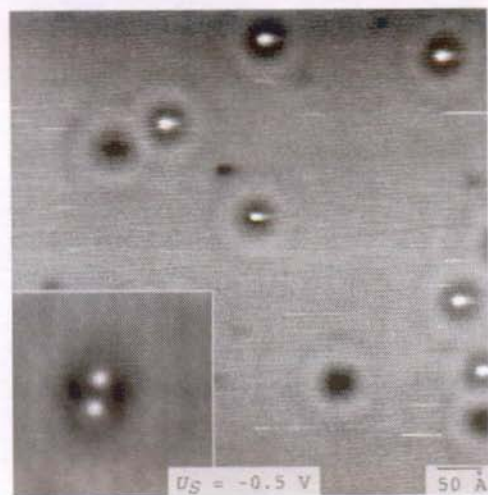


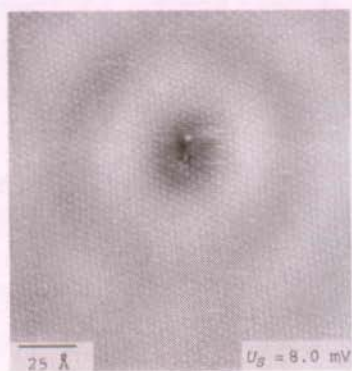
Figure 5.4: Standing waves around impurity atoms. ($T = 5$ K)

The nature of the point defects has been discussed in literature [70, 64]. In our case they are not due to monatomic vacancies in the top surface layer, but presumably consist of bulk contaminants (Sulfur or carbon) which diffuse to the surface during annealing of the sample. From Figure 5.4 it is evident that at least two different types of contaminants are present. Depending on their chemical nature they can cause a depletion or an increase of the electron density at the adsorption site. Note that the impurity level in the previous images is extremely low. The density of scatterers in Figure 5.2 for example corresponds to an impurity concentrations of only $2 \cdot 10^{-4}$. Figure 5.5 shows two examples. In (a) the substitution of a silver atom by a contaminant decreases the local density of states at E_F whereas in (b) the vicinity of the contaminant reveals a higher LDOS at E_F .

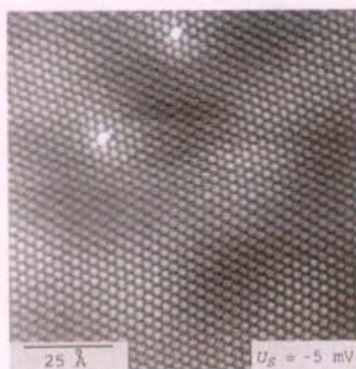
5.2 The surface state dispersion relation

Standing electron waves are characterized by a periodic modulation of the electron density of the surface state. They are created by the interference between a wave incident onto a step and a second wave that has been reflected by this step. The wave length is therefore a characteristic value for the momentum k_{\parallel} of the surface state electrons. By measuring simultaneously k_{\parallel}

a)



b)



c)

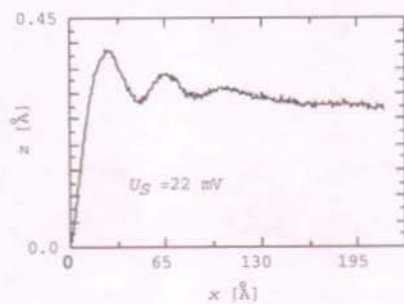


Figure 5.5: a)/b) Atomic resolution images of impurities on the surface. c) A topographic line scan starting at the adsorption site of an impurity atom. ($T = 5$ K)

and the energy E of a standing wave it is consequently possible to determine the dispersion relation of the surface state. As explained in chapter 2 it would not be sufficient to measure the tunneling current in order to determine the local density of states ρ_S since this would integrate over all electronic states that are accessible by the applied voltage. The result would be a complicated interference pattern of waves with many different wave lengths. One is therefore obliged to measure the derivative dI/dV for all allowed energy values of the surface state.

A frequently used technique to do so is to modulate the tunneling voltage by a small sinusoidal voltage at a frequency sufficiently higher than the feedback response time. By measuring the tunneling current component at the modulation frequency one gets a two dimensional representation of the electron density of states at the tunneling bias. However, the difficulty arises that the tip-sample distance in the vicinity of a scatterer is not constant. The reason is that the feedback control is always adjusting the tunneling barrier in order to obtain a constant tunneling current. In other words the feedback control will interfere with the simultaneous dI/dV -measurement by causing the tip to follow the electronic corrugation of the surface.

Feenstra, Stroscio, and Fein [71] proposed to overcome this problem by normalizing the dI/dV values by I/V . This technique gave satisfactory results in a study of the Si(111) (2×1) surface. Yet it is not clear if this calculation is applicable to all systems. In a numerical study of the imaging of the surface state of Cu(111) by STM Hörmandinger [72] came to the conclusion that both $(dI/dV)/I/V$ and dI/dV representations exhibit similar deviations from the density of surface states in the case where the tunneling constant is held constant (constant current mode).

The most simple and exact way to measure the dispersion relation is therefore to apply a tunneling voltage in a range where electrons from the surface state do not contribute significantly to the tunneling current. Then the constant current mode will keep the tip at a constant height above the surface. In order to determine the local density of states at a certain potential the scanning motion of the tip is stopped, the feedback loop is opened and the dI/dV value at the corresponding potential can be measured. Obviously, this scheme requires a high stability of the tunneling barrier while the feedback loop is opened. Li *et al.* [69] note that a voltage where surface state contributions to the tunneling current are negligible cannot be known *a priori*. However, it can be measured easily. One can either take a dI/dV -spectrum on the surface in order to determine the surface state energy distribution or one searches by trial-and-error for a voltage where no height modulations

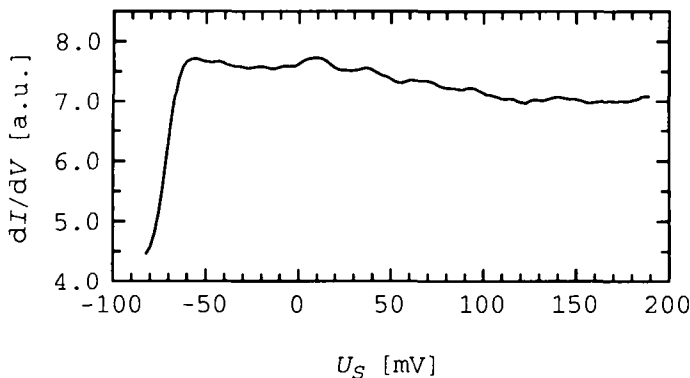


Figure 5.6: dI/dV -spectrum on a clean Ag(111) surface. ($T \approx 5$ K)

around scattering centers are observable in the topographic image.

In order to find an appropriate tunneling potential we first measure the density of states distribution of the surface state. The corresponding dI/dV -spectrum is shown in Figure 5.6. It has been taken on a clean terrace far away from steps and impurities. The onset of the surface state is found to be at 65 meV below the Fermi energy. At this voltage the contribution from the surface state is about 50 percent of the total conductance. Increasing the bias potential to higher voltages above the Fermi level reduces the conductance. This behavior shows that the surface state does not form an ideal 2D free electron gas that would have a constant density of states above its onset energy. From the spectrum in Figure 5.6 we can derive a tunneling voltage that should be well suited to guarantee a constant distance between the sample surface and the tip. Potentials lower than -0.5 V or higher than 0.5 V turned out to be appropriate. The line scan in Figure 5.7 gives an example. In this case a tunneling voltage of 0.5 V omits any measurable height modulations on the terraces near a monatomic step.

With these prerequisites in hand we can now measure the electron dispersion relation of the surface state. The measurement scheme is as follows: At each point of the line scan the feedback loop is opened and a complete dI/dV -spectrum is taken. After the readjustment of the tunneling voltage the feedback loop is closed and the tip is moved to the next pixel position. This procedure is repeated for every point of the line scan. Electron density modulations caused by the electron standing waves can be recovered from

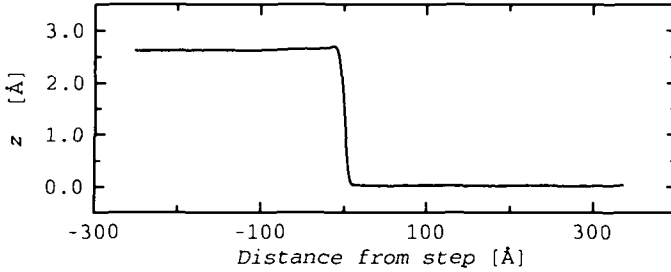


Figure 5.7: Topographic line scan at a monatomic step on Ag(111). By choosing a tunneling bias of 0.5 V current contributions from the surface state becomes negligible and the terraces appear flat even at scattering centers. ($T = 5$ K)

these measurements by comparing the intensity of the dI/dV -spectra at the different points of the line scan. For this purpose the dI/dV value is shown in a grey scale representation in Figure 5.8 as a function of the distance from the step and the tunneling voltage V . Each pixel is the average from two consecutive voltage sweeps. Thereby each horizontal line scan of this plot shows the spatial modulations of the electron density at one selected energy E with respect to E_F . The experiment has been carried out at 5 K.

Crommie, Lutz, and Eigler [64] found the k_{\parallel} vector that corresponds to a certain energy by fitting the dI/dV spectra at this energy to a zero-order Bessel function which contains k_{\parallel} as a fitting parameter. In principle this technique can now be applied to each of the horizontal line scans of the plot in Figure 5.8. However, in the aim to improve the quality of the fit we averaged over an energy interval of ten neighbored energy values for each fit. As an example the result of such a fit around a tunneling potential of 8.5 mV is shown in Figure 5.9.

The obtained set of (k_{\parallel}, E) pairs is plotted in Figure 5.10. The dispersion relation $E(k_{\parallel})$ has a clear minimum at $k_{\parallel}=0$ and increases monotonically with increasing momentum. The results can be well fitted to a free-electron-like dispersion relation with an effective mass m^* describing the motion of the electron parallel to the surface:

$$E(k_{\parallel}) = E_0 + \frac{\hbar^2 k_{\parallel}^2}{2m^*}, \quad (5.1)$$

where E_0 is the energy of the surface state band edge.

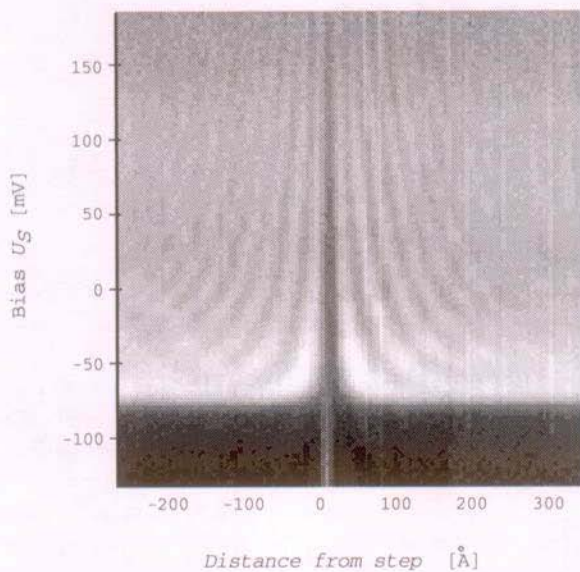


Figure 5.8: Electron density distribution as a function of the distance from a step and of the tunneling voltage U_S . Note that a vertical line scan in this plot is equivalent with the spectrum in Figure 5.6. ($T = 5$ K)

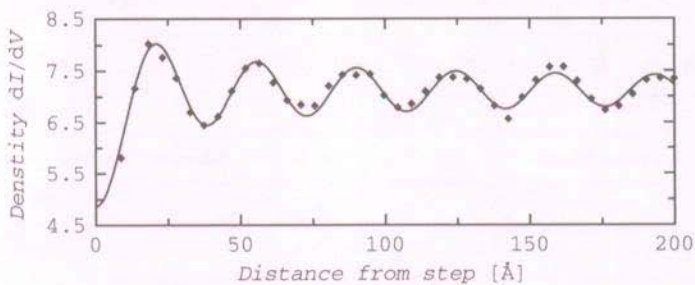


Figure 5.9: Zero-order Bessel function fitted to the data of the plot in Figure 5.8.

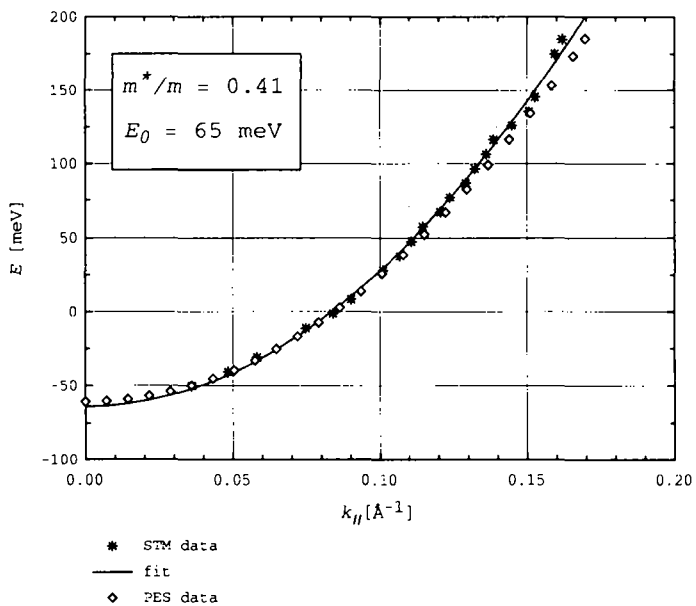


Figure 5.10: Dispersion relation of the surface state on Ag(111). The diamonds indicate results obtained from photoemission experiments in reference [61].

	PES	STM
m^*/m	0.44	0.41
E_0 [meV]	61 meV	65 meV

Table 5.1: Comparison of the effective mass and onset energy of the surface state determined by photoemission [61] and tunneling spectroscopy.

For comparison the dispersion relation from the photoemission measurement of reference [61] is shown as well. From the numerous photoemission studies this reference has been chosen since the experiments were performed at low temperatures allowing for a more exact determination of the Fermi energy E_F than measurements at room temperature. From the parabolic fit to the experimental values one obtains the results summarized in table 5.1. The results from photoemission spectroscopy and tunneling spectroscopy agree very well. Furthermore the results are in accordance with other recently published tunneling measurements from Li *et al.*. This is of particular interest since in literature values of the onset energy E_0 between -120 meV and -40 meV [73, 74, 61] have been reported from photoemission experiments. The discrepancy has been assigned to the difficulty in PES to determine the Fermi energy when the measurements are carried out at room temperature. Therefore the results from low temperature experiments as shown in table 5.1 should represent the most exact values available to date.

5.3 Spatially confined surface states

In the preceding section it has been shown that the surface state electrons form a two-dimensional quasi-free electron state. This results from the dispersion relation that describes the motion of a free electron with the effective mass m^* and the particular density of states. In order to determine the momentum of an electron with energy E we made use of the partial reflection of an electron wave incident onto a surface defect and the formation of a standing wave pattern in the vicinity of the scattering center. It is therefore not surprising that the electron density of states can become discrete when the scatterer is assembled in a way where it confines the free electrons into lateral dimensions of the order of their de Broglie wavelength. Such experiments have been performed both on natural surface defects such as steps and small 2D islands on the (111) surfaces of Cu, Au and Ag [69, 75, 76] and on artificially created, so-called quantum corral structures that have been assembled by means of the tunneling tip of the STM [30, 31, 65]. In these cases



Figure 5.11: Topographical image of the confinement structure.

the electrons have been confined either in two dimensions by the formation of a closed loop (quantum corrals, 2D islands) or only in one dimension by scattering at a pair of parallel steps.

In the following I will describe the confinement of surface state electrons by a pair of parallel steps separated by 51 Å. The geometry of the scatterer can be seen in Figure 5.11. A similar situation has before been studied by Avouris and Lyo [76] on Au(111) at room temperature.

In order to find the allowed energy levels of the surface state electrons one separates the wave function into two directions parallel and orthogonal to the steps. In the direction perpendicular to the steps the situation is equivalent to a "particle-in-a-box" problem. Since the boundary conditions impose a vanishing density of states at the step edges standing waves that allow only for a discrete set of energy values are formed. Parallel to the steps the electrons are free to move and the resulting wave functions are plane waves. Since in this direction all energy values are allowed the corresponding energy spectrum will be continuous. However, the density of states of a one dimensional free electron gas is not a constant as in the case of the infinite 2D surface state electron gas. In one dimension the density of states is proportional to $(E - E_1)^{-1/2}$, where E_1 is the lowest energy value of the system. In the present case E_1 is the onset energy of the *confined* surface

state.

The total two dimensional density of states should therefore show a sharp onset at E_1 . Increasing the energy should lead to a more continuous decrease of the density of states until the next resonance of the motion perpendicular to the steps is reached. In other words the discrete energy levels of the perpendicular motion are broadened by the continuous contribution to the density of states from the motion of the electrons parallel to the steps.

To verify this explanation we carried out an experiment similar to the one presented in Figure 5.8. During one scan oriented perpendicular to the steps one takes dI/dV spectra at each location of the tip.

Figure 5.12 shows a grey scale representation of dI/dV as a function of the location x and the energy E with respect to E_F . The abscissa of the plot denotes the spatial position of the tunneling tip between the steps and the ordinate the selected energy of the respective dI/dV line scan.

Increasing the tunneling potential from about -100 mV leads at -46 meV to the formation of a first maximum along the line scan. This maximum is due to the lowest order electron standing wave that is allowed in the potential barrier. The onset energy of the confined state has shifted by approximately +20 meV with respect to the quasi free electron gas.

Further increasing of the bias potential leads to the formation of two maxima in the line scan at about 32 mV, to three maxima at about 164 mV and at more than 300 mV to four maxima. Higher order maxima have not been observed since the signal-to-noise ratio became too small. On the lower end of the spectrum at voltages lower than -46 meV the step edges appear bright. This effect is due to the local modification of the tunneling barrier at step edges and is not caused by the confinement of surface state electrons [76].

The width of the first maximum is approximately 65 meV. The broadening is due to the above described one dimensional contribution to the density of states from the motion parallel to the steps and to the finite reflectivity of the step edges. The cross-section in Figure 5.13 shows that the evolution of the electron density of the first maximum as a function of energy. As theoretically expected the increase is indeed much sharper than the decrease that should follow the $(E - E_1)^{-1/2}$ dependence. Other broadening contributions (the finite lifetime of an electron in the barrier and the modulation technique of the dI/dV measurement) play therefore apparently only a minor role.

The reflection of the electron wave at both steps of the terrace creates a sinusoidal standing wave in the direction perpendicular to the steps. From the boundary condition $d/\lambda = n\pi$ follows that only energy values are allowed

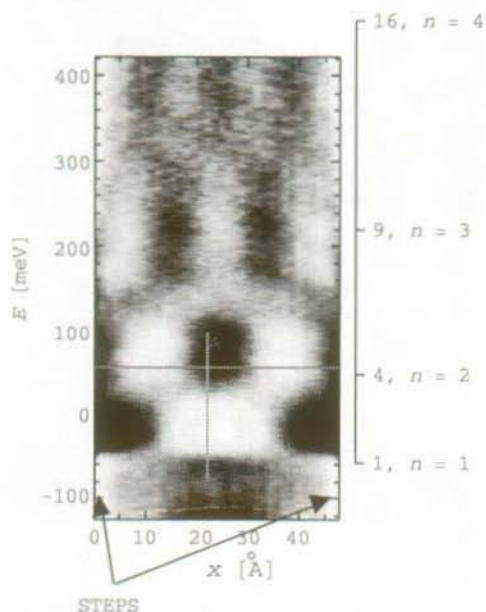


Figure 5.12: Electron density distribution in the direction perpendicular to the confining Ag-steps. The cross-sections A and B are shown in the Figures 5.13 and 5.14, respectively. ($T = 5$ K)

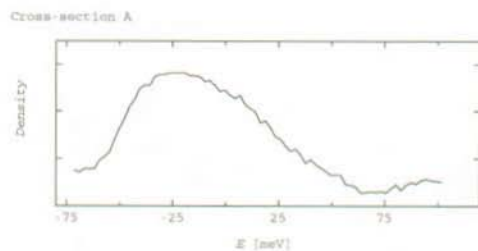


Figure 5.13: Density of states as indicated by cross-section A in Figure 5.12 showing a sharp increase at the onset energy of the confined surface state.

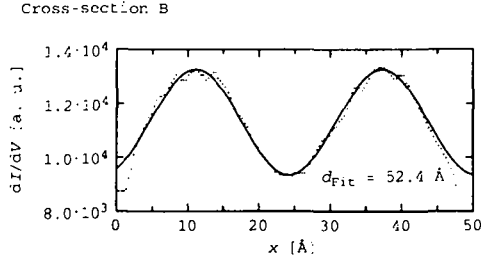


Figure 5.14: Sinusoidal fit to the experimental data for the electron standing wave with $n = 2$ as indicated by cross-section B in Figure 5.12.

that obey the equation,

$$E_n = \frac{\pi^2 \hbar^2}{2m^* d^2} n^2, \quad (5.2)$$

where E_n is the n -th energy eigenvalue and d the width of the potential. Energy values that have been calculated from equation (5.2) are also shown in Figure 5.12. In the lowest orders estimated and measured values agree approximately. However, from the third order on the experimental values are shifted to lower energies than theoretically expected. This might not be very surprising since the assumption of infinite rectangular potential barriers is not fulfilled in reality. The change of the barrier form causes a deviation from the simple n^2 proportionality and can therefore account for the observed behavior. Nevertheless the linescan in Figure 5.14 shows that the second order standing wave between the steps can be fitted by a sinusoidal wave function. The effective width of the terrace obtained from the fit is 52.4 Å in good agreement with the topographical value of 51 Å.

The above experiment shows a simple example how the confinement of the 2D surface state in a further dimension parallel to the surface leads to a modified wave function that can be separated into two independent directions: Perpendicular to the confining surface steps the electron density of states becomes discrete whereas parallel to the steps a continuous, one dimensional behavior is found. Since scanning tunneling spectroscopy measures the local density of states a direct two dimensional representation of the solution can be found. In the future it will be possible to study more complicated surface structures and the influence of a magnetic field on the interference pattern of surface state electrons.

Chapter 6

Ni islands on Ag(111)

It is well known from both photoemission spectroscopy (PES) and scanning tunneling spectroscopy (STS) studies that the surface state is sensitive to changes in the morphological and the chemical properties of the surface. Since the surface state electrons are localized in a plane close to the surface, it is obvious that they might be sensitive to any surface contamination. This problem has already been addressed in PES experiments by Gartland and Slagsvold [60] who found a high sensitivity of the surface state on Cu(111) on oxygen contamination. Li [70] recognized by scanning tunneling spectroscopy that the surface state on Ag(111) can locally be destroyed by the adsorption of single Ag atoms. The destruction is in this case induced by the local perturbation of the potential periodicity. Consequently, on silver islands with dimensions of the order of the de Broglie wavelength of the surface state electrons the surface state reappears. Calculations by Hörmandinger and Pendry showed that the scattering behavior of surface state electrons depend both on the morphology and the chemical nature of adatoms on the surface. While the reflectivity of Cu or Fe rows on a Cu(111) surface is limited mainly by their rather high transmissivity for an incident electron wave, it is the scattering into bulk states that limits the reflectivity of adsorbed S and C rows on the surface. In the following the influence of adsorbed nickel islands on the surface state will be characterized.

A further motivation to study this system was however, to verify whether the magnetic moment of the Ni atoms has an influence on the electronic sample properties. For certain alloys containing a small amount of magnetic impurities it is well known that the spin-spin interaction between the impurities and the conduction electrons can cause the resistivity of the sample to *increase* at low temperatures. This is the so-called Kondo effect. In a pure metal the resistivity decrease with decreasing temperature since scattering



Figure 6.1: Submonolayer growth of Ni on Ag(111) at 130 K. The image has been taken at 77 K.

off phonons becomes less probable at low temperatures. In an alloy electron scattering off magnetic impurities can cause the electron's spin to flip. This effect is at the origin of the resistance increase at low temperatures (typically $T \leq 10$ K). Since the scattering causes the electron density to decrease at the Fermi energy E_F the Kondo scattering can be detected by a dip in the conductance spectra around zero energy.

6.1 The structure of Ni islands on Ag(111)

Figure 6.1 gives an example of a submonolayer amount of Ni evaporated at low temperature (130 K) onto the Ag(111) surface. As this temperature is sufficiently high to overcome the surface diffusion barrier, adsorbed nickel atoms diffuse on the surface as long as they get captured by other diffusing atoms in order to form stable islands. The islands formed in Figure 6.1 are, however, not yet compact but show a ramified form. Several island branches point in directions turned by 120° with respect to each other indicating the preferential growth directions which are imposed by the underlying substrate.

From studies of metal growth on close-packed hexagonal surfaces the ex-

istence of a preferential growth direction often results in dendritic growth of the islands at low temperature. Such a behavior has been observed both in homoepitaxy [77, 78] and heteroepitaxy [79]. In the system of Ag/Pt(111) the dendritic growth has been proven to be caused by different corner diffusion barriers for a Ag atom to diffuse from the corner to an A-step or a B-step of the island, respectively.

Nickel islands prepared at low temperature on Ag(111) are mostly ramified as well. As occasionally almost compact islands can be observed the diffusion barrier asymmetry seems not to be as pronounced as in the case of Ag on Pt(111).

The width of the island branches reaches several nanometers. This indicates that edge diffusion along the nickel islands is not completely suppressed even at 130 K.

Several islands in Figure 6.1 have already started to grow in the second layer. Upon deposition at 300 K one finds islands with a compact form and some of them having a height corresponding to two Ni monolayers (see Figure 6.2). This implies necessarily that Ni atoms jump from the substrate onto a Ni island. A similar behavior has previously been observed in the growth of Co on Au(111) and Cu(111) [80, 81, 82]. For the system of Ni/Au(111) [83] growth in the second layer has been reported to start only in later growth stages (> 0.6 ML). We can therefore conclude that Ni on Ag(111) grows preferentially in three dimensions. Apparently, the jump of a Ni atom on Ag(111) onto a Ni adislands is prohibited at 130 K since the corresponding energy barrier is too high. Raising the temperature to 300 K this process becomes possible.

Before turning to the spectroscopic measurements the morphology of the islands shall be further clarified. The system of Ni/Ag(111) is characterized by a large lattice misfit of 14 % ($d_{Ni} = 2.49$ Å and $d_{Ag} = 2.89$ Å). The growth of such a system can in principle occur in two distinct ways. In systems where the surface potential created by the substrate is highly corrugated and dominates over the interactions within the adsorbate the periodicity of the substrate often forces the adsorbate to grow pseudomorphically. In systems with rather small adsorbate-substrate interactions the adsorbate cannot be forced into registry with the substrate and is then free to relax growing in its natural morphology. The latter incommensurate growth scheme is found preferentially in physisorbed systems. Novaco and McTague [84, 85] showed that the strain energy depends not only on the lattice mismatch but also on the relative orientation of the substrate and the overlayer.

Pseudomorphic growth of the nickel islands would – due to the large

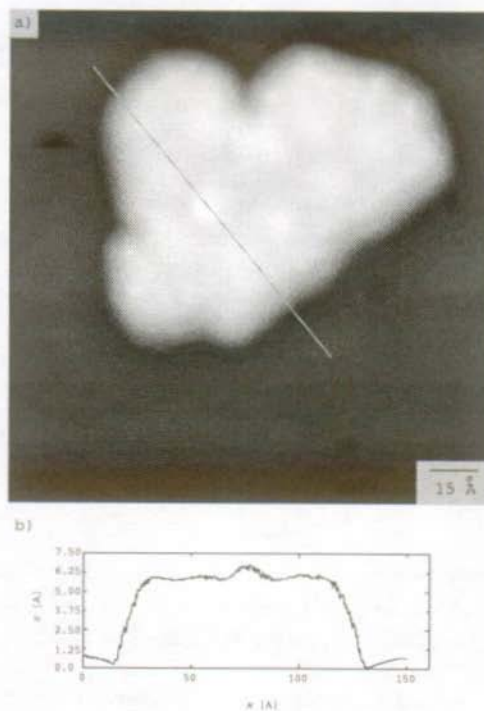


Figure 6.2: a) Ni island on Ag(111) prepared at 285 K. b) Cross-section as indicated in a). The height of 5.7 Å corresponds to two Ni layers.

misfit – require a highly corrugated adsorbate-substrate potential for nickel atoms on the silver surface in order to overcome the interaction potential between neighbored nickel atoms within an island. Yet, the high mobility of nickel atoms even at low-temperatures suggests that this condition might not be fulfilled. Therefore one can expect that the lateral adatom distance is governed by the dominating interaction between the adsorbate atoms. Figure 6.3 shows a nickel island of monatomic height on Ag(111) that has been grown at 130 K. Hexagonally arranged height maxima are observed on top of the island. They can be interpreted as a moiré pattern that arises from incommensurate adsorption sites of nickel atoms on the substrate. The distance d_m between two height maxima is 19.7 Å (see the cross-section in (b)).

The periodicity of the moiré pattern is for itself not sufficient to clarify the adsorption geometry of the Ni atoms since still the rotational angle is unknown. This angle can be determined from atomic resolution images such as the one shown in Figure 6.4. The moiré is modulated by height oscillations of higher frequency that is caused by single Ni atoms. The nearest neighbor distance d_{Ni} between the Ni atoms is measured to be 2.50 Å which comes close to the corresponding value of bulk nickel of 2.49 Å.

From Figure 6.4 also the rotational angle of the nickel lattice with respect to the substrate lattice can be determined. Since the angle α between the atomic rows of the substrate and the overlayer does not depend very sensitively on the angle β between the Ni atom rows and the moiré superlattice it is favorable (and less difficult) to measure the latter angle in order to determine the exact adsorption geometry. From the measurement one obtains $\beta = 46^\circ$. As can be found from Figure 6.5 the angles α and β are related to each other by

$$\tan \alpha = \frac{\|\vec{g}_m\| \sin \beta}{\|\vec{g}_{Ni}\| - \|\vec{g}_m\| \cos \beta} = \frac{\sin \beta}{-\cos \beta + d_m/d_{Ni}}, \quad (6.1)$$

where \vec{g}_m , \vec{g}_{Ni} are the reciprocal lattice vectors of the moiré pattern and the overlayer and d_m , d_{Ni} the nearest neighbor distances, respectively. For small angles equation 6.1 simplifies to

$$\beta = \frac{d_m - d_{Ni}}{d_{Ni}} \alpha. \quad (6.2)$$

From equation (6.1) one obtains $\alpha = 5.9^\circ$. Table 6.1 summarizes all structure parameters of the Ni islands on Ag(111). It should be noted that the actual angle between the Ni overlayer and the moiré pattern can vary substantially. The influence on the angle α is however small since the reciprocal lattice

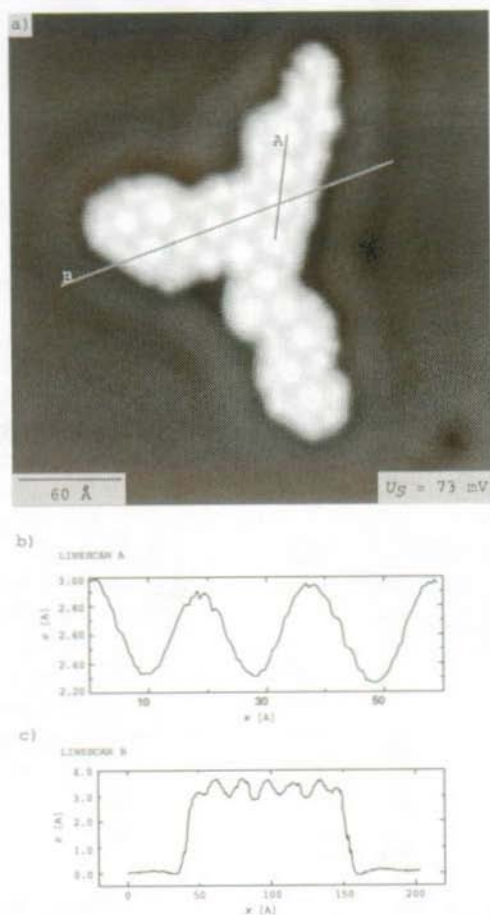


Figure 6.3: a) Ni island on Ag(111) prepared at 130 K. b) Linescan A showing the height modulations of the moiré pattern ($d_m = 19.7 \text{ Å}$). c) Linescan B revealing the monatomic height.

$d_{Ni} [\text{Å}]$	$\beta [^\circ]$	$\alpha [^\circ]$
2.5	46	5.9

Table 6.1: Structure parameters of a Ni islands on Ag(111).

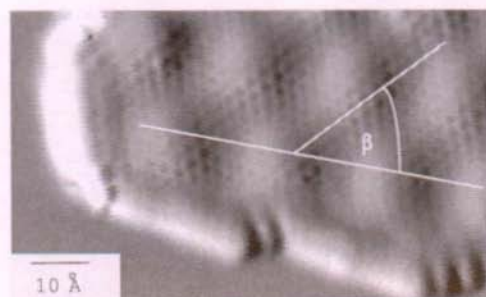


Figure 6.4: Atomic resolution image of a Ni island on Ag(111) (dz/dx representation). The nearest neighbor distance of Ni $d_{Ni} = 2.5 \text{ \AA}$. The angle between the Ni rows and the moiré pattern β is 46° .

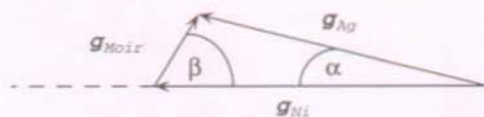


Figure 6.5: Reciprocal lattice vectors of the substrate, the Ni overlayer and the moiré pattern, respectively. Adopted from [86].

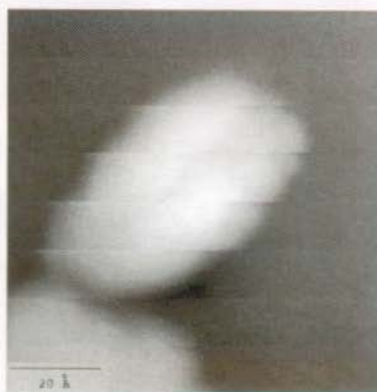


Figure 6.6: A Ni island on Ag(111). The tunneling spectra shown in Figure 6.7 are taken on top of the island (a) and in its vicinity at a distance of approximately 20 Å (b).

vector of the moiré pattern is short with respect to the reciprocal vectors of the substrate and the overlayer.

6.2 Tunneling spectra on Ni islands

From the image in Figure 6.3 one can see that Ni islands are surrounded by a standing wave pattern on the underlying Ag substrate. In this sense there is no difference to silver adislands on the surface. However, there is apparently no standing electron wave on top of the island. In the aim to confirm this observation we recorded dI/dV tunneling spectra on the islands and at several distances in the vicinity of the Ni island shown in Figure 6.6. The spectrum in Figure 6.7 (a) has been taken on top near the center of the Ni island. The electron density is almost constant in the entire energy range. So, apparently, there is no surface state on the Ni island. The spectrum shown in (b) of Figure 6.7 is the average of ten spectra taken in the vicinity of the Ni island at a distance of 20 Å. Here the well known surface state is fully developed. The spectra therefore confirm the observation that has already been drawn from the topographical image. The electronic modification of the surface properties leads to the destruction of the surface state. However, since both the morphological and the chemical structure are locally changed we have no means to decide which modification causes the surface state to disappear.

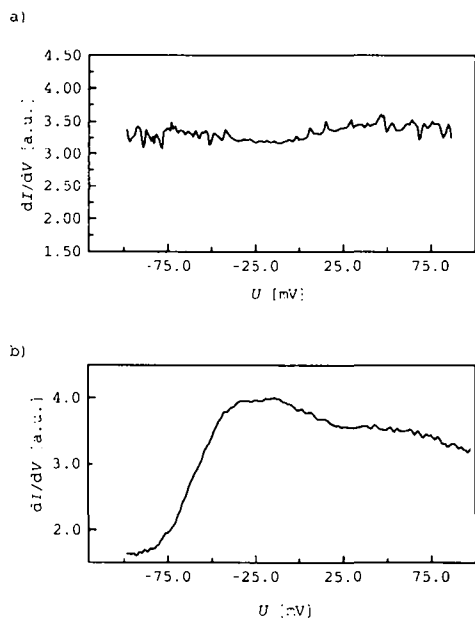


Figure 6.7: Spectra of the density of states on top of the Ni island in Figure 6.6 and in its vicinity acquired at $T = 5$ K. a) On top. b) At a distance of 20 Å from the Ni island edge on the Ag(111) substrate.

A gap in the density of states distribution that one would expect in a Kondo system could not be observed. Neither the spectrum in Figure 6.7 (a) shows any anomalies around zero energy nor the one in Figure 6.7 (b). Calculations of the electronic structures of impurities from first principles [87] showed that Ni atoms are nonmagnetic when embedded in a silver crystal. One might consequently suspect that in our case the magnetic moment of Ni is quenched as well. This would explain why no Kondo behavior has been found.

Chapter 7

Outlook

The characterization of the LTSTM in chapters 3 and 4 shows that the mechanical stability of the LTSTM is very high allowing a topographical z-resolution in the range of $1/1000 \text{ \AA}$. In the lateral direction atomic resolution can be obtained routinely. The mechanical properties and the low drift at low temperatures will allow to investigate electronic properties of nanoscopic surface structures. A good starting point will be a more detailed study of the surface state properties:

- In the present thesis the scattering of surface state electrons off surface defects has been studied in zero magnetic field. For the future it would be interesting to investigate how the electron's behavior can be influenced by destroying the energy degeneration of spin-up and spin-down electrons in a magnetic field. One expects that the distinct dispersion relation for spin-up and spin-down electrons leads to a spatial beating of the electron standing wave near a surface step and thereby to a faster decay of the wave as a function of the distance from the step.
- The oscillations of the local density of states near a surface step at 5 K can be approximated by a zeroth order Bessel function. At elevated temperatures the coherence of the electrons will be destroyed by coupling to phonons. Measuring the decay of the standing wave as function of temperature can be employed to determine the change of the electron coherence length. This would provide information on how electrons couple to phonons at the surface. Since the current STM design does not allow for active temperature control such a measurement has to be performed during a warm-up period of the cryostat. Experience shows that thermal drift is not increased significantly at temperatures up to 80 K.

Quantum size effects are another interesting subject. An example has been given in section 5.3 by a pair of parallel steps causing the density of state spectrum to become discrete in the confined direction. More interestingly, STM can be employed to investigate electron states in nanoscopic particles by tunneling spectroscopy. As has been outlined in the introduction, the influence of the substrate on the particle has to be reduced by a double barrier tunneling set-up. This is particularly important for the investigation of superconducting properties since the coupling to a normal conducting substrate would hinder the superconducting transition to occur. A promising system might be the adsorption of a superconducting metal on an oxidized NiAl crystal. Diffraction as well as STM measurements have shown that on this sample a native, two monolayer thick crystalline oxide layer can be prepared that can be imaged with atomic resolution [88, 89]. This oxide layer provides one tunneling barrier between the substrate and the metal particle while the second barrier is established by the vacuum between the particle and the tip. Such a measurement scheme would offer the possibility to investigate the superconductivity of the particles as a function of their shape and size.

Tunneling spectroscopy is also suited to investigate magnetic properties. Tunneling spectra obtained by Yazdani *et al.* [7] near magnetic adsorbates on a superconducting Nb sample showed the presence of excitations within the energy gap of the superconductor. Control measurements near adsorbed Ag atoms did not reveal any influence on the density of states. It is therefore possible to distinguish magnetic from nonmagnetic adsorbates by tunneling spectroscopy. The magnetic moment is detected in an indirect manner by its influence on the superconductor's density of states. By using a superconducting tip the aforementioned effect could be applied to all kinds of substrates (normal or superconducting) in the aim to investigate the magnetism of adsorbates.

These examples demonstrate how tunneling spectroscopy can expand the capabilities of the STM from merely imaging morphological surface properties to the investigation of physical properties that are not only interesting for their own sake but that are of technological relevance in the future.

References

- [1] W. P. Halperin, Rev. Mod. Phys. **58**, 533 (1986).
- [2] P. W. Anderson, J. Phys. Chem. Solids **11**, 26 (1959).
- [3] I. Giaever and H. R. Zeller, Phys. Rev. Lett. **20**, 1504 (1968).
- [4] J. M. Blatt and C. J. Thompson, Phys. Rev. Lett. **10**, 332 (1963).
- [5] C. J. Thompson and J. M. Blatt, Phys. Lett. **5**, 6 (1963).
- [6] R. Meservey and P. M. Tedrow, Phys. Rep. **238**, 173 (1994).
- [7] A. Yazdani, B. A. Jones, C. P. Lutz, M. F. Crommie, and D. M. Eigler, Science **275**, 1767 (1997).
- [8] D. C. Ralph, C. T. Black, and M. Tinkham, Phys. Rev. Lett. **74**, 3241 (1995).
- [9] C. T. Black, D. C. Ralph, and M. Tinkham, Phys. Rev. Lett. **76**, 688 (1996).
- [10] G. Binnig, H. Rohrer, C. Gerber, and E. Weibel, Phys. Rev. Lett. **49**, 57 (1982).
- [11] P. J. M. van Bentum, H. van Kempen, L. E. C. van de Leemput, and P. A. A. Teunissen, Phys. Rev. Lett. **60**, 369 (1988).
- [12] P. J. M. van Bentum, R. T. M. Smokers, and H. van Kempen, Phys. Rev. Lett. **60**, 2543 (1988).
- [13] K. Mullen, E. Ben-Jacob, and S. Ruggiero, Phys. Rev. B **38**, 5150 (1988).
- [14] R. Wilkins, E. Ben-Jacob, and R. C. Jaklevic, Phys. Rev. Lett. **63**, 801 (1989).

- [15] K. A. McGreer, J.-C. Wan, N. Anand, and A. M. Goldman, *Phys. Rev. B* **39**, 12260 (1989).
- [16] D. M. Eigler and E. K. Schweizer, *Nature* **344**, 524 (1990).
- [17] J. Bardeen, L. N. Cooper, and J. R. Schrieffer, *Phys. Rev.* **108**, 1175 (1957).
- [18] R. H. Fowler and L. Nordheim, *Proc. Roy. Soc. A* **119**, 173 (1928).
- [19] J. Tersoff and D. R. Hamann, *Phys. Rev. Lett.* **50**, 1998 (1983).
- [20] J. Tersoff and D. R. Hamann, *Phys. Rev. B* **31**, 805 (1985).
- [21] J. Bardeen, *Phys. Rev. Lett.* **6**, 57 (1961).
- [22] C. J. Chen, *J. Vac. Sci. Technol. A* **9**, 44 (1990).
- [23] E. L. Wolf, *Principles of Electron Tunneling Spectroscopy* (Oxford University Press, New York, 1985).
- [24] S. Kashiwaya and M. Koyanagi, *J. Phys. Soc. Jap.* **63**, 3098 (1994).
- [25] C. Renner, Ph.D. thesis, Université de Genève, 1993.
- [26] S. il Park and R. C. Barrett, *Methods of Experimental Physics* (Academic Press, New York, 1993).
- [27] M. Okano, K. Kajimura, S. Wakiyama, F. Sakai, W. Mizutani, and M. Ono, *J. Vac. Sci. Technol. A* **5**, 3313 (1987).
- [28] J. Frohn, J. F. Wolf, K. Besocke, and M. Teske, *Rev. Sci. Instrum.* **60**, 1200 (1989).
- [29] S. Behler, M. K. Rose, D. F. Ogletree, and M. Salmeron, *Rev. Sci. Instrum.* **68**, 124 (1997).
- [30] M. F. Crommie, C. P. Lutz, and D. M. Eigler, *Science* **262**, 218 (1993).
- [31] M. F. Crommie, C. P. Lutz, D. M. Eigler, and E. J. Heller, *Physica D* **83**, 98 (1995).
- [32] Newport, Fontaine Valley, CA, USA.
- [33] Oxford Instruments, Eynsham, England.
- [34] Lakeshore, Westerville, OH, USA.

- [35] Epoxy Technology, Billerica, MA, USA.
- [36] K. Besocke, *Surf. Sci.* **181**, 145 (1987).
- [37] C. Rossel, R. R. Schulz, and G. Romano, *Cryogenics* **33**, 1161 (1993).
- [38] R. R. Schulz and C. Rossel, *Rev. Sci. Instrum.* **65**, 1918 (1994).
- [39] S. J. Stranick and P. S. Weiss, *Rev. Sci. Instrum.* **65**, 918 (1994).
- [40] S. J. Stranick, M. M. Kamna, and P. S. Weiss, *Rev. Sci. Instrum.* **65**, 3211 (1994).
- [41] G. N. Henderson, P. N. First, T. K. Gaylord, E. N. Glytsis, B. J. Rice, P. L. Dantzcher, D. K. Guthrie, L. E. Harrell, and J. S. Cave, *Rev. Sci. Instrum.* **66**, 91 (1995).
- [42] G. Meyer, *Rev. Sci. Instrum.* **67**, 2960 (1996).
- [43] H. Röder, Ph.D. thesis, Ecole Polytechnique Fédérale de Lausanne, 1994.
- [44] B. Gasser, A. Menck, H. Brune, and K. Kern, *Rev. Sci. Instrum.* **67**, 1925 (1996).
- [45] M. H. Jericho, D. C. Dahn, and B. L. Blackford, *Rev. Sci. Instrum.* **58**, 1349 (1987).
- [46] B. Fischer, Ph.D. thesis, Ecole Polytechnique Fédérale de Lausanne, 1998.
- [47] D. W. Pohl, *IBM J. Res. Develop.* **30**, 417 (1986).
- [48] Y. S. Touloukian and C. Y. H. eds., *Thermophysical Properties of Matter* (Purdue Research Foundation, New York, 1970).
- [49] R. David, K. Kern, P. Zeppenfeld, and G. Comsa, *Rev. Sci. Instrum.* **57**, 2771 (1986).
- [50] STM 200 from RHK Technology, Rochester Hills, MI, USA.
- [51] M. Poza, J. G. Rodrigo, and S. Vieira, *Physica B* **218**, 265 (1996).
- [52] G. Binnig, H. Rohrer, C. Gerber, and E. Weibel, *Surf. Sci. Lett.* **131**, L379 (1983).

- [53] K.-M. Ho and K. P. Bohnen, *Phys. Rev. Lett.* **59**, 1833 (1987).
- [54] T. Gritsch, D. Coulman, R. J. Behm, and G. Ertl, *Surf. Sci.* **257**, 297 (1991).
- [55] EBL No.1 from Staveland Sensors, East Hartford, CT, USA.
- [56] M. B. Hugenschmidt, A. Hitzke, and R. J. Behm, *Phys. Rev. Lett.* **76**, 2535 (1996).
- [57] M. B. H. M. Ruff, A. Hitzke, and R. J. Behm, *Surf. Sci.* **388**, L110 (1997).
- [58] I. Tamun, *Physik. Zeits. Sowjetunion* **1**, 733 (1932).
- [59] W. Shockley, *Phys. Rev.* **56**, 317 (1939).
- [60] P. O. Gartland and B. J. Slagsvold, *Phys. Rev. B* **12**, 4047 (1975).
- [61] R. Panagio, R. Matzdorf, G. Meister, and A. Goldmann, *Surf. Sci.* **336**, 113 (1995).
- [62] L. C. Davis, E. P. Everson, R. C. Jaklevic, and W. Shen, *Phys. Rev. B* **43**, 3821 (1991).
- [63] Y. Hasegawa and P. Avouris, *Phys. Rev. Lett.* **71**, 1071 (1993).
- [64] M. F. Crommie, C. P. Lutz, and D. M. Eigler, *Nature* **363**, 524 (1993).
- [65] E. J. Heller, M. F. Crommie, C. P. Lutz, and D. M. Eigler, *Nature* **369**, 464 (1994).
- [66] P. Avouris, I.-W. Lyo, and P. Molinàs-Mata, *Chem. Phys. Lett.* **240**, 423 (1995).
- [67] D. Fujita, K. Amemiya, T. Yakabe, H. Nejoh, T. Sato, and M. Iwatsuki, *J. Vac. Sci. Technol. A* **15**, 1613 (1997).
- [68] D. Fujita, K. Amemiya, T. Yakabe, H. Nejoh, T. Sato, and M. Iwatsuki, *Phys. Rev. Lett.* **78**, 3904 (1997).
- [69] J. Li, W.-D. Schneider, and R. Berndt, *Phys. Rev. B* **56**, 1 (1997).
- [70] J. T. Li, Ph.D. thesis, Université de Lausanne, 1997.
- [71] R. M. Feenstra, J. A. Stroscio, and A. P. Fein, *Surf. Sci.* **181**, 295 (1987).

- [72] G. Hörmandinger, *Phys. Rev. B* **49**, 13897 (1994).
- [73] G. V. Hansson and S. A. Flodström, *Phys. Rev. B* **18**, 1572 (1978).
- [74] K. Giessen, F. Hage, F. J. Himpsel, H. J. Riess, and W. Steinmann, *Phys. Rev. Lett.* **55**, 300 (1985).
- [75] J. M. Garcia, O. Sanchez, P. Segovia, J. E. Ortega, J. Alvarez, A. L. V. de Parga, and R. Mirande, *Appl. Phys. A* **61**, 609 (1995).
- [76] P. Avouris and I.-W. Lyo, *Science* **264**, 942 (1994).
- [77] M. Hohage, M. Bott, M. Morgenstern, Z. Zhang, T. Michely, and G. Comsa, *Phys. Rev. Lett.* **76**, 2366 (1996).
- [78] H. Brune, H. Röder, C. Boragno, and K. Kern, *Phys. rev. B* **49**, 167 (1994).
- [79] K. Bromann, Ph.D. thesis, Ecole Polytechnique Fédérale de Lausanne, 1997.
- [80] B. Voigtländer, G. Meyer, and N. M. Amer, *Phys. Rev. B* **44**, 10354 (1991).
- [81] C. Tölkes, P. Zeppenfeld, M. A. Krzyzowski, R. David, and G. Comsa, *Phys. Rev. B* **55**, 13932 (1997).
- [82] J. de la Figuera, J. E. Prieto, C. Ocal, and R. Miranda, *Phys. Rev. B* **47**, 13043 (1993).
- [83] D. D. Chambliss, R. J. Wilson, and S. Chiang, *Phys. Rev. Lett.* **66**, 1721 (1991).
- [84] A. D. Novaco and J. P. McTague, *Phys. Rev. Lett.* **38**, 1286 (1977).
- [85] J. P. McTague and A. D. Novaco, *Phys. Rev. B* **19**, 5299 (1979).
- [86] T. Wiederholt, H. Brune, J. Wintterlin, R. J. Behm, and G. Ertl, *Surf. Sci.* **324**, 91 (1995).
- [87] R. Podloucky, R. Zeller, and P. H. Dederichs, *Phys. Rev. B* **22**, 5777 (1980).
- [88] R. M. Jäger, H. Kuhlenbeck, H.-J. Freund, M. Wuttig, W. Hoffmann, R. Franchy, and H. Ibach, *Surf. Sci.* **259**, 235 (1991).

- [89] J. Libuda, F. Winkelmann, M. Bäumer, H.-J. Freund, T. Bertram, H. Neddermeyer, and K. Müller, *Surf. Sci.* **318**, 61 (1994).

Curriculum vitae

1968	Born in Grünstadt, Germany
1979–1988	Staatl. Leininger Gymnasium, Grünstadt
1988	Abitur
1988–1994	Study of Physics at Rheinische Friedrich-Wilhelms-Universität Bonn
1993–1994	Diploma work at Ecole Polytechnique Fédérale de Lausanne on “Molekulare Ordnung und Morphologie von Alkanthiol-monolagen auf Au(111)”
1994–1997	Ph. D. student at Ecole Polytechnique Fédérale de Lausanne under the supervision of Prof. Dr. K. Kern
1998	Ph. D. thesis on “Low Temperature Scanning Tunneling Microscopy and Spectroscopy in Ultra-High-Vacuum and High Magnetic Fields”

Remerciements

J'aimerais remercier en premier lieu le Professeur Klaus Kern, mon directeur de thèse, pour m'avoir donné l'opportunité de réaliser ce travail, pour son engagement et son optimisme pendant cette période.

Ensuite j'aimerais remercier tout ceux qui ont pris part au projet. Avec Harri Brune j'ai souvent eu l'occasion de discuter des plans de constructions du microscope et des problèmes techniques qui surgissent au cour d'un tel projet. Je remercie tout particulièrement mes collègues Lukas Bürgi et Olivier Jeandupeux qui ont collaboré avec moi pendant le montage et la mise au point de l'expérience. Merci pour votre enthousiasme et votre soutien à la fin de ce projet.

Je tiens aussi à remercier l'équipe de l'atelier qui a très largement contribué très fortement au succes du projet. Tout d'abord un grand merci à Philippe Zurcher qui a fait la plupart des pièces ainsi qu'à Claude Blanc, Philippe Cordey, Michel Fazan, Gilles Grandjean et André Schlaefli. Un Merci particulier à André Guisolan, Dédé, pour son engagement et sa disponibilité tout au long du projet.

Je voudrais aussi remercier Wolfgang Harbich et Harald Jödicke, spécialistes dans la Physique à basse température, pour leurs conseils dans ce domaine.

Au-delà du projet j'aimerais remercier tous ceux qui ont créer une ambiance agréable et amicale. En particulier, j'aimerais mentionner Ornella Cavalleri et Alexander Menck, mes complices au bureau et dans ma vie lausannoise.

Finalement je remercie le Studienfonds der Basler Chemischen Industrie pour son soutien financier.

L'achèvement de cette thèse a été rendu possible graces aux auberges Bürgi, Jeandupeux, Kind et Menck.